

Global ITG eigenmodes: From ballooning angle and radial shift to Reynolds stress and nonlinear saturation

Cite as: Phys. Plasmas **27**, 072507 (2020); <https://doi.org/10.1063/5.0006765>

Submitted: 05 March 2020 . Accepted: 21 June 2020 . Published Online: 15 July 2020

J. Zielinski , M. Becoulet, A. I. Smolyakov , X. Garbet , G. T. A. Huijsmans , P. Beyer, and S. Benkadda



View Online



Export Citation



CrossMark

ARTICLES YOU MAY BE INTERESTED IN

[Role of sheared \$E \times B\$ flow in self-organized, improved confinement states in magnetized plasmas](#)

Phys. Plasmas **27**, 060501 (2020); <https://doi.org/10.1063/1.5142734>

[A new explanation of the sawtooth phenomena in tokamaks](#)

Phys. Plasmas **27**, 032509 (2020); <https://doi.org/10.1063/1.5140968>

[An improved theory of the response of DIII-D H-mode discharges to static resonant magnetic perturbations and its implications for the suppression of edge localized modes](#)

Phys. Plasmas **27**, 072501 (2020); <https://doi.org/10.1063/5.0011738>



NEW!

Sign up for topic alerts
New articles delivered to your inbox

Global ITG eigenmodes: From ballooning angle and radial shift to Reynolds stress and nonlinear saturation

Cite as: Phys. Plasmas **27**, 072507 (2020); doi: 10.1063/5.0006765

Submitted: 5 March 2020 · Accepted: 21 June 2020 ·

Published Online: 15 July 2020



View Online



Export Citation



CrossMark

J. Zielinski,^{1,a)} M. Becoulet,² A. I. Smolyakov,¹ X. Garbet,² G. T. A. Huijsmans,³ P. Beyer,⁴ and S. Benkadda⁴

AFFILIATIONS

¹University of Saskatchewan, S7N 5E2 Saskatoon, Canada

²CEA/IRFM, 13115 Cadarache, France

³ITER Organization, 13115 Saint Paul Lez Durance, France

⁴Aix-Marseille Université, CNRS, PIIM UMR 7345, 13397 Marseille, France

^{a)} Author to whom correspondence should be addressed: j.zielinski@usask.ca

ABSTRACT

We present global linear and nonlinear simulations of ion temperature gradient instabilities based on a fluid formulation, with an adapted version of the JOEK code. These simulations are performed in realistic global tokamak equilibria based on the solution of the Grad-Shafranov equation. Benchmarking of linear growth rates was successfully completed with respect to previously published data. We find two distinct types of eigenstructures, depending on the magnetic shear. For high shear, when the coupling of poloidal harmonics is strong, ballooning-type eigenmodes are formed, which are up-down asymmetric with a finite ballooning angle, θ_0 . The poloidal harmonics which form the global eigenmode are found to demonstrate a radial shift, being centered well outside of their corresponding rational surface. Stronger diamagnetic effects increase both θ_0 and proportionately shift the m harmonics to larger radii (by as much as two rational surfaces). In the low shear regime, the unstable eigenmodes become narrowly localized between neighboring pairs of rational surfaces, and exhibit no up-down asymmetry. Our simulations also show the generation of finite Reynolds stress due to nonlocal/global profile effects. This stress possesses both poloidally symmetric ($n = m = 0$) and asymmetric (finite- m) components. Turbulent saturation in nonlinear simulations is demonstrated for both shear regimes.

Published under license by AIP Publishing. <https://doi.org/10.1063/5.0006765>

I. INTRODUCTION

Ion Temperature Gradient (ITG) instabilities are a dominant contributor to the turbulent ion energy losses in tokamaks. Although the simplest ITG modes can be obtained in a local approximation, full solutions for unstable ITG modes are sensitive to global profiles and magnetic geometry effects. Shear flows, up-down asymmetry in divertor configurations, and nonlocal effects arising from magnetic shear, plasma density, and temperature profiles lead to nontrivial global eigenmodes,^{1–3} e.g., up-down asymmetric modes centered away from the outboard midplane and rotated by the so-called ballooning angle, $\theta_0 \neq 0$. In local flux-tube simulations, a finite value of θ_0 can be introduced as an external parameter which maximizes the growth rates,^{4,5} so that θ_0 is the expected location for the most unstable local mode. Profile and finite θ_0 effects have been investigated within generalized 2D ballooning theory.^{1,6,7} Global solutions can be built from local (flux

tube) simulations, in which the higher order effects are captured by the finite ballooning angle found from 2D analytical theory.^{3,5,8,9} Global profiles and shear flow effects on micro-instabilities have been studied with global electrostatic gyrokinetic codes, such as LORNB5,¹⁰ GYSELA,^{11–13} and others.^{14–19} It has also been shown that the nontrivial nature of global eigenmodes, in particular the broken symmetry, strongly influences the Reynolds stress generation from such modes.^{1,3,7,8,20,21} All such effects are important for edge plasmas and Edge Localized Mode (ELM) dynamics,²² particularly for divertor configurations near the separatrix,² resonant interactions with external magnetic perturbations,^{23,24} transport barrier formation,^{25–29} and more generally, for the excitation of microinstabilities in configurations with magnetic islands.³⁰

The goal of this work is to study linear and nonlinear micro-instabilities, particularly ITGs, in global magnetic field and plasma

pressure configurations. We have been developing global simulations of ITG turbulence using an electrostatic adaptation of the JOREK code, which is a global finite element fluid code originally designed for simulations of ELMs in complete X-point geometry. The implementation of this electrostatic fluid description of ITG modes into JOREK takes advantage of the previous extensive development of the code with respect to equilibrium, geometry, and numerical methods, which were originally applied to MHD simulations. In particular, the realistic equilibrium obtained from the Grad-Shafranov solver, flux-aligned grid needed for modeling, and all numerical developments of the sparse matrix solver were used here. These features allow us to consider the excitation and interaction of ITG modes across many rational surfaces, along with including macroscopic tokamak phenomena. In this paper, we first demonstrate successful benchmarking to the linear growth rate data in Refs. 31 and 32. Although our equilibria are poloidally symmetric, these simulations do indeed develop the up-down asymmetry in the mode structure, enumerated by the finite ballooning angle, $\theta_0 \neq 0$. In varying the magnetic shear, while maintaining the same temperature gradients, we have shown a transition from the typical global ballooning mode structure, where $\theta_0 > 0$, to modes which are radially localized between adjacent rational surfaces, which retain their up-down symmetry, $\theta_0 = 0$, as is typical for slab-like modes. The transition to localized modes occurs for low values of magnetic shear, $\bar{s} = d(\ln q)/d(\ln r) \lesssim 0.7$ (where q is the safety factor and r is the minor radius), at which the elongated ballooning structure breaks down due to weaker coupling between poloidal harmonics.

In this paper, we also study the structure of the quasilinear Reynolds stress, which arises due to global geometric effects. Reynolds stress drives plasma rotation, and can lead to the generation of poloidal shear flows, which have been shown to suppress turbulent transport by stretching and breaking apart turbulent vortices.³³ This limits the spatial scale over which the vortices can transfer energy, resulting in turbulent self-stabilization. If the flows become strong enough, they can lead to the formation of transport barriers, which are most likely responsible for the transition between low and high confinement regimes (L-mode and H-mode, respectively). Transport barrier formation is commonly studied in the context of zonal flows, which are poloidally and toroidally symmetric flows, $n = m = 0$, however there is growing interest in poloidally asymmetric flows (convective cells), which have been detected experimentally.³⁴ In particular, the $m = 1$ component of the turbulent Reynolds stress is of interest for the generation of Geodesic Acoustic Modes (GAMs).

It has been pointed out that the eigenmode asymmetries (i.e., ballooning angle) predicted within the generalized 2D ballooning theory can also lead to significant residual Reynolds stress.^{1,20,21} Generalized ballooning theory, which includes global profile effects, also predicts a combined monopole $m = 0$ and $m = 1$ dipole structure of the Reynolds stress, even in poloidally symmetric equilibria.^{1,3,6,35} In this paper, we investigate these mechanisms by studying the poloidal structure of the Reynolds stress depending on the value of the magnetic shear and demonstrate significant generation of Reynolds stress due to magnetic shear, diamagnetic, and global profile effects.

Mode saturation in multi-harmonic simulations of multiple $n > 0$ is also demonstrated and analyzed. This occurs for all shear configurations, however, the resultant energy level distribution of each constituent n harmonic can be markedly different. Furthermore, for low shear configurations, we find the possibility of nonlinear

saturation in single- n simulations (without coupling to $n = 0$), occurring by the coupling of unstable *poloidal* harmonics to stable ones. This occurs since we use a non-Boussinesq form of the vorticity³⁶ which leads to cubic interactions between three variables, allowing a single toroidal mode n to couple to itself.

In Sec. II, we describe the two constituent components of our ITG model, and describe their linear analytic behavior. Following this, in Sec. III we briefly overview JOREK, the code we use for the simulation, outline our calculation of equilibrium, and describe the combined nonlinear model used in simulations. Section IV, describes our benchmarking comparisons to existing simulations, and Sec. V offers a thorough analysis of the two distinct mode types which arise in simulations of a single toroidal mode number. Section VI then investigates the Reynolds stress of each of these mode types. Section VII covers the nonlinear behavior in our simulations, beginning by discussing saturation occurring via coupling between m modes, then moving on to turbulent states including multiple $n > 0$ modes. Finally, we conclude in Sec. VIII by offering a summary of our results.

II. LINEAR ITG THEORY

There are two main types of ITG modes, commonly referred to as the toroidal^{37–40} and slab^{41–44} ITGs. Both modes are driven by negative effective compressibility, where an increase in density occurs with a decrease in pressure ($\partial p_i / \partial n_i < 0$, where p_i and n_i are the ion pressure and density, respectively). The toroidal ITG (tITG) mode is an interchange mode, and is thus only unstable in a particular configuration—namely, when a force is directed against a density gradient. The prototypical example of an interchange mode is the Rayleigh Taylor instability, where for a heavy fluid above a light one, the downward force of gravity is directed opposite the upward density gradient. Conceptually, this mechanism is the fluid equivalent of a pendulum in an inverted state. For the tITG, the force is provided by the magnetic gradient and curvature, and this force opposes the density gradient on the low field side, in the so-called “unfavorable curvature” region.

For the slab ITG (sITG) mode, different contributions of the parallel and perpendicular fluxes can result in negative effective compressibility. When the gradient in temperature surpasses the gradient in density, a region can experience a net inflow of pressure, being carried most rapidly perpendicular to the magnetic field, while the net flux of density is negative, being carried mostly rapidly parallel to the field. This allows local changes in density and pressure to be of opposite sign, and thus $\partial p_i / \partial n_i < 0$.

In our model, stabilization of short wavelengths is provided by ion inertia. This effect results in an ion sound Larmor radius term, which stabilizes the mode at a high $k_\perp \rho_i$ (where k_\perp is the perpendicular wavenumber and ρ_i the ion gyroradius). In the present work, we ignore the consideration of ion Landau damping, which can be included later using an appropriate closure relation.^{45,46}

A. Toroidal ITG

We begin our derivation of the tITG by considering the electron dynamics, which is governed by the electrostatic parallel electron momentum balance in which inertia is ignored

$$0 = en_e \nabla_\parallel \tilde{\phi} - \nabla_\parallel \tilde{p}_e. \quad (1)$$

Here, n_e (later n_i) is the electron (ion) number density, ϕ is the potential, p_e (later p_i) is the electron (ion) pressure, and in the local model,

∇_{\parallel} is the derivative along z . This approximation is valid for the low frequency regime, $\omega \ll k_z v_{Te}$ (where k_z is the wave number along the magnetic field direction and v_{Te} (later v_{Ti}) the electron (ion) thermal velocity), and treats the electrons as adiabatic, resulting in the Boltzmann relation

$$\tilde{n}_e = \frac{1}{\tau} \frac{e\tilde{\phi}}{T_{i0}} n_0, \quad (2)$$

where $\tau = T_{e0}/T_{i0}$ is a constant based on centerline temperatures, n_0 is the equilibrium density, and the over-tilde is used to highlight some of the fluctuating quantities (mainly variables).

To describe the ion dynamics, we utilize the ion continuity and energy equations

$$\frac{\partial n_i}{\partial t} + \nabla \cdot [n_i(\mathbf{v}_E + \mathbf{v}_{pi})] + n_{i0} \nabla \cdot \mathbf{v}_{ii} = 0, \quad (3)$$

$$\frac{\partial p_i}{\partial t} + \mathbf{v}_E \cdot \nabla p_i + \frac{5}{3} p_i \nabla \cdot (\mathbf{v}_E + \mathbf{v}_{pi}) + \frac{2}{3} \nabla \cdot \mathbf{q} = 0, \quad (4)$$

where $n_{i0} = n_0$ is the equilibrium ion density, and \mathbf{q} is the heat flux. The $\mathbf{E} \times \mathbf{B}$, diamagnetic, and inertial drifts are

$$\mathbf{v}_E = \frac{\hat{\mathbf{b}} \times \nabla \tilde{\phi}}{B}, \quad \mathbf{v}_{pi} = \frac{\hat{\mathbf{b}} \times \nabla p_i}{en_i B}, \quad \mathbf{v}_{ii} = \frac{1}{\omega_{ci}} \hat{\mathbf{b}} \times \frac{d_0}{dt} \mathbf{v}_E,$$

respectively, and have been obtained from the perpendicular momentum equation assuming $\omega \ll \omega_{ci}$ (ω_{ci} the ion cyclotron frequency) and $d_0/dt = \partial/\partial t + \mathbf{v}_E \cdot \nabla$ is the convective derivative including only the $\mathbf{E} \times \mathbf{B}$ drift. Note that we have used the Boussinesq approximation in (3), which omits density convection by the inertial drift. Furthermore, for the meantime, the diamagnetic drift is neglected within the inertial drift, however, it will be included later in the nonlinear JOREK system via the gyroviscous cancelation.⁴⁷ This system of equations is supplemented using quasineutrality $n_e = n_i$, and the diamagnetic heat flux,⁴⁸ $\mathbf{q} = \mathbf{q}^{(0)}$

$$\mathbf{q}^{(0)} = \frac{5}{2} \frac{p_i}{eB_0} \hat{\mathbf{b}} \times \nabla T_i. \quad (5)$$

It is important to note that this closure includes only fluid effects, and thus the effect of ion Landau damping is not investigated at this time. This model for tITGs is quite similar to the Weiland model,^{39,40} which has been used extensively in ITG investigations.

Using local slab coordinates (x radial, y poloidal, and z along \mathbf{B}), and the normalized variables $\Phi = e\tilde{\phi}/T_{i0}$, $P = \tilde{p}_i/p_{i0}$, the continuity and energy equations become

$$\frac{1}{\tau} \frac{\partial \Phi}{\partial t} - \tau \rho_s^2 \frac{\partial}{\partial t} \nabla_{\perp}^2 \Phi = v_{*i} \frac{\partial \Phi}{\partial y} - \mathbf{v}_{Di} \cdot \nabla (\Phi + P), \quad (6)$$

$$\frac{\partial P}{\partial t} = (1 + \eta_i) v_{*i} \frac{\partial \Phi}{\partial y} - \frac{5}{3} \mathbf{v}_{Di} \cdot \nabla \left[\Phi \left(1 - \frac{1}{\tau} \right) + 2P \right], \quad (7)$$

where the magnetic curvature and gradient drift, and the equilibrium diamagnetic drift are

$$\mathbf{v}_{Di} = \frac{2T_i}{eB} (\hat{\mathbf{b}} \times \nabla \ln B), \quad \mathbf{v}_{*i} = \frac{T_i}{eB} \frac{\partial (\ln n_{i0})}{\partial x},$$

respectively, $\eta_i = \partial \ln T_{i0} / \partial \ln n_{i0}$, and $\rho_s^2 = T_e m_i / e^2 B^2$, is the ion sound Larmor radius. Here, the terms proportional to v_{*i} originate

from the $\mathbf{E} \times \mathbf{B}$ advection of density and pressure, whereas those proportional to \mathbf{v}_{Di} originate from the divergence of the $\mathbf{E} \times \mathbf{B}$ and diamagnetic drifts, along with $\nabla \cdot \mathbf{q}^{(0)}$. Note that due to quasineutrality and our use of adiabatic electrons, the continuity equation now appears as an equation for potential.

Neglecting the inertial term, proportional to ρ_s^2 , and considering plane waves, this system can be reduced to the dispersion relation

$$\omega = \frac{5}{3} \omega_{Di} + \frac{\tau}{2} (\omega_{Di} - \omega_{*i}) \pm \sqrt{\tau \omega_{Di} \omega_{*i} (\eta_{cr} - \eta_i)}, \quad (8)$$

where $\omega_{Di} = v_{Di} k_y$, $\omega_{*i} = v_{*i} k_y$ (k_y is the wavenumber in the y direction), and

$$\eta_{cr} = \frac{2}{3} + \frac{\tau}{4} \left(\frac{\omega_{Di}}{\omega_{*i}} + \frac{\omega_{*i}}{\omega_{Di}} - 2 \right) + \frac{10}{9\tau} \frac{\omega_{Di}}{\omega_{*i}}. \quad (9)$$

Thus, the tITG system is unstable for $\eta_i > \eta_{cr}$.

B. Slab ITG

As with the tITG, we consider adiabatic electrons for the sITG, as defined in (2). We neglect the toroidal effects, provided by the diamagnetic drifts, and instability is now provided via parallel ion motion, which is included by incorporating the parallel ion velocity, $\tilde{v}_{i\parallel}$, and the parallel ion momentum equation

$$\frac{\partial n_i}{\partial t} + \nabla \cdot [n_i(\mathbf{v}_E + \tilde{v}_{i\parallel} \hat{\mathbf{b}})] + n_i \nabla \cdot \mathbf{v}_{ii} = 0, \quad (10)$$

$$\frac{\partial p_i}{\partial t} + (\mathbf{v}_E + \tilde{v}_{i\parallel} \hat{\mathbf{b}}) \cdot \nabla p_i + \frac{5}{3} p_i \nabla \cdot (\mathbf{v}_E + \tilde{v}_{i\parallel} \hat{\mathbf{b}}) = 0, \quad (11)$$

$$n_i m_i \frac{\partial \tilde{v}_{i\parallel}}{\partial t} + (\mathbf{v}_E + \tilde{v}_{i\parallel} \hat{\mathbf{b}}) \cdot \nabla \tilde{v}_{i\parallel} = -en_i \nabla_{\parallel} \tilde{\phi} - \nabla_{\parallel} \tilde{p}_i. \quad (12)$$

The same simplifications for \mathbf{v}_E occur as in the tITG, and $\tilde{v}_{i\parallel}$ is retained as a variable. Utilizing the normalized variable $V_{i\parallel} = \tilde{v}_{i\parallel}/v_{Ti}$, along with Φ and P as before, results in the linearized system

$$\frac{1}{\tau} \frac{\partial \Phi}{\partial t} - \frac{\rho_s^2}{\tau} \frac{\partial}{\partial t} \nabla_{\perp}^2 \Phi = v_{*i} \frac{\partial \Phi}{\partial y} - v_{Ti} \frac{\partial V_{i\parallel}}{\partial z}, \quad (13)$$

$$\frac{\partial P}{\partial t} = (1 + \eta_i) v_{*i} \frac{\partial \Phi}{\partial y} - \frac{5}{3} v_{Ti} \frac{\partial V_{i\parallel}}{\partial z}, \quad (14)$$

$$\frac{\partial V_{i\parallel}}{\partial t} = -v_{Ti} \frac{\partial \Phi}{\partial z} - v_{Ti} \frac{\partial P}{\partial z}. \quad (15)$$

Although the tITG mechanism is easily visualized through the Rayleigh–Taylor instability, the sITG is not so simple. Nevertheless, insight into how instability arises within the sITG can be found by expanding the spatial components of these equations onto a Fourier basis. This yields

$$\frac{\partial \Phi}{\partial t} = i v_{*i} k_y \Phi - i v_{Ti} k_z V_{i\parallel}, \quad (16)$$

$$\frac{\partial P}{\partial t} = i(1 + \eta_i) v_{*i} k_y \Phi - i \frac{5}{3} v_{Ti} k_z V_{i\parallel}, \quad (17)$$

$$\frac{\partial V_{i\parallel}}{\partial t} = -i v_{Ti} k_z (\Phi + P), \quad (18)$$

where we have ignored inertia and consider $\tau = 1$ for simplicity. For a positive perturbation in potential and pressure, i.e., a locally increased

ion density, (18) shows that the ions will spread away along the field lines, departing from the considered region. The corresponding decreases in density and pressure are encapsulated in the rightmost terms in (16) and (17). Note that these first two equations are nearly identical, except for the factors of $(1 + \eta_i)$, and $5/3$ in the pressure equation (17). For $(1 + \eta_i) = 5/3$ these two equations will yield differing rates of change in density and pressure, however, they can certainly not take on different signs (what is needed for a negative compressibility instability). Considering, now, $(1 + \eta_i) > 5/3$, and all terms on the right hand side being positive, we see that the time rate of change in pressure can, in fact, take on a different sign than the time rate of change in density, which is proportional to Φ . This is the source of the instability.

To see how this occurs practically, consider Fig. 1, in which $(1 + \eta_i) > 5/3$, and there is a positive perturbation in ion density (and subsequently potential and pressure). This perturbation results in the formation of a $E \times B$ vortex, owing to the first term on the right-hand side of (16) and (17). On the lower part of this vortex, since the pressure gradient is larger than the density gradient, more pressure will be convected into the area than density—to make this clear, we can imagine the density gradient as vanishingly small, thus eliminating the density convection entirely. At the same time, density leaves the region along the field line. Thus, the lower part of the vortex experiences increasing pressure (from the $E \times B$ convection) and decreasing density (from the parallel motion)—negative compressibility. In the case when the density gradient is finite, the situation simply amounts to the net change in pressure being positive, due to its $E \times B$ convection into the region outpacing its parallel motion out of it, while the net change in density is negative, due to its parallel motion outpacing its $E \times B$ convection.

The system of equations defined by (13)–(15) can be reduced to the following dispersion relation:

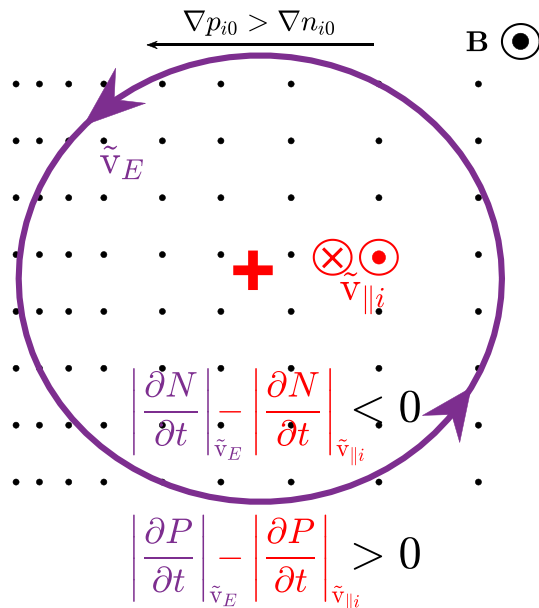


FIG. 1. Schematic of the sITG mechanism (see the text for description). Note, $N = \tilde{n}_i/n_{i0} \sim \Phi$ is only used in this image— Φ is the main variable.

$$\omega \left[\frac{\omega}{k_{\parallel}^2 v_{Ti}^2} \left(\frac{\omega}{\tau} + \omega_{*i} \right) - 1 \right] - \frac{5}{3} \frac{\omega}{\tau} + \left(\eta_i - \frac{2}{3} \right) \omega_{*i} = 0. \quad (19)$$

In the limit of $k_{\parallel} v_{Ti} \ll 1$, the cubic term dominates, and we are left with

$$\omega^3 + k_{\parallel}^2 v_{Ti}^2 \tau (\eta_i - 2/3) \omega_{*i} = 0. \quad (20)$$

This is always unstable, provided $\eta_i \neq 2/3$, as is the case for common fluid models of the sITG,^{41,42} unlike the critical thresholds for the sITG which arise in kinetic models.^{43,44}

C. Linear analysis of the general model

The general ITG model is composed of both the tITG and sITG mechanisms, and is given by

$$\frac{\partial n_i}{\partial t} + \nabla \cdot \left[n_i (\mathbf{v}_E + \mathbf{v}_{pi} + \tilde{v}_{i\parallel} \hat{\mathbf{b}}) \right] + n_{i0} \nabla \cdot \mathbf{v}_{ii} = 0, \quad (21)$$

$$\begin{aligned} \frac{\partial p_i}{\partial t} + (\mathbf{v}_E + \tilde{v}_{i\parallel} \hat{\mathbf{b}}) \cdot \nabla p_i \\ + \frac{5}{3} p_i \nabla \cdot (\mathbf{v}_E + \mathbf{v}_{pi} + \tilde{v}_{i\parallel} \hat{\mathbf{b}}) = -\frac{2}{3} \nabla \cdot \mathbf{q}, \end{aligned} \quad (22)$$

$$n_i m_i \frac{\partial \tilde{v}_{i\parallel}}{\partial t} + (\mathbf{v}_E + \tilde{v}_{i\parallel} \hat{\mathbf{b}}) \cdot \nabla \tilde{v}_{i\parallel} = -e n_i \nabla \tilde{\phi} - \nabla_{\parallel} \tilde{p}_i, \quad (23)$$

along with (1) and quasineutrality. The linearized system is given by

$$\frac{1}{\tau} \frac{\partial \Phi}{\partial t} - \frac{\rho_s^2}{\tau} \frac{\partial}{\partial t} \nabla_{\perp}^2 \Phi = v_{*i} \frac{\partial \Phi}{\partial y} - \mathbf{v}_{Di} \cdot \nabla (\Phi + P) - v_{Ti} \frac{\partial V_{i\parallel}}{\partial z}, \quad (24)$$

$$\begin{aligned} \frac{\partial P}{\partial t} = (1 + \eta_i) v_{*i} \frac{\partial \Phi}{\partial y} \\ - \frac{5}{3} \mathbf{v}_{Di} \cdot \nabla \left[\Phi \left(1 - \frac{1}{\tau} \right) + 2P \right] - \frac{5}{3} v_{Ti} \frac{\partial V_{i\parallel}}{\partial z}, \end{aligned} \quad (25)$$

$$\frac{\partial V_{i\parallel}}{\partial t} = -v_{Ti} \frac{\partial \Phi}{\partial z} - v_{Ti} \frac{\partial P}{\partial z}. \quad (26)$$

For local analysis, we select

$$k_z = -\frac{x}{L_s} k_y, \quad (27)$$

as is geometrically appropriate for slab coordinates ($ik_z = \hat{\mathbf{b}} \cdot \nabla$), where x is the distance from the rational surface, $L_s = Rq/\hat{s}$ is the magnetic shear length, and $\hat{s} = \partial \ln q / \partial \ln r$ is the magnetic shear. We estimate an appropriate distance x , using a relevant simulation presented later in Fig. 5(a). It will be shown that in this case (which is the most radially localized global mode), the mode appears directly between two rational surfaces, at a distance of $x = 1$ cm from each of them.

Since k_x only appears within k_{\perp} , and subsequently only leads to mode stabilization through the ion sound Larmor radius term, we utilize the value $k_x = 0$. With these values, along with $q = 1.4$, $R = 171$ cm, and $\hat{s} = 1/2$, the growth rate and frequency of the local tITG, sITG, and ITG models are shown in Fig. 2. We can see that the general ITG behavior is dominated by the tITG, with some competition in mode growth⁴⁹ arising from the slab mechanism. The frequency of the general mode is, however, larger than that of both tITG and sITG, and increases for increasing magnetic shear. The magnetic shear only effects the sITG components (via the determination of

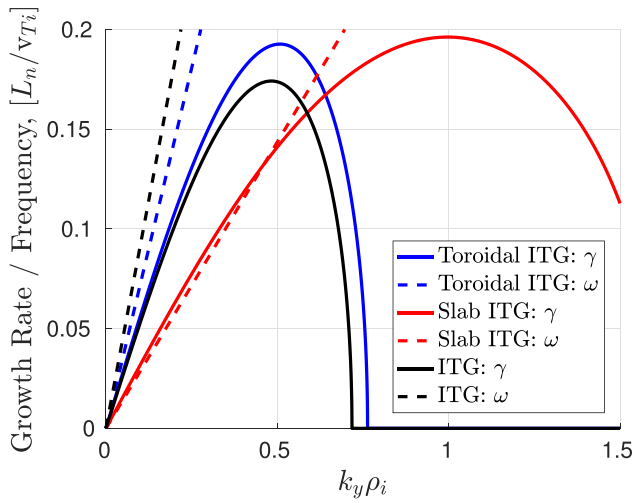


FIG. 2. Analytical growth rate and frequency of tITG, sITG, and ITG models. Normalized with $v_{Ti} = 4.48 \times 10^5$ m/s and $L_n = 76.6$ cm.

k_z), and the sITG is stable as $\hat{s} \rightarrow 0$, where the growth rate curve is flattened to larger $k_y \rho_i$, and for $\hat{s} \geq 1.2$, where the region of instability is pushed toward the origin. This behavior affects the ITG mode differently, for which the overall behavior approaches that of the tITG in the limit $\hat{s} \rightarrow 0$, whereas for $\hat{s} \geq 1.3$, the ITG is stabilized.

III. THE JOREK CODE

JOREK was designed to simulate large-scale MHD phenomena, such as edge-localized modes and disruptions in realistic tokamak geometry.^{50–52} JOREK simulates the complete tokamak domain (including the scrape-off-layer) by using Fourier decomposition in the toroidal direction, and the finite element method in the poloidal plane. Each element is decomposed on the basis of cubic Hermite polynomials, which allow for accurate representations of the variables and their second order derivatives on the scale of the grid size. For the purpose of this investigation, we have adapted the code to simulate our two-fluid model at scales relevant to ITG microturbulence.

A. Equilibrium in JOREK

Before the numerical simulation of our ITG equations can begin, an equilibrium state must be defined. JOREK uses a built-in equilibrium solver which calculates a full MHD equilibrium, utilizing the Grad-Shafranov equation

$$R \frac{\partial}{\partial R} \left(\frac{1}{R} \frac{\partial \psi}{\partial R} \right) + \frac{\partial^2 \psi}{\partial Z^2} = -P_f \mu_0 R^2 p'(\psi) - \mu_0^2 F(\psi) F'(\psi). \quad (28)$$

This equation is represented in the poloidal plane with coordinates R and Z , where the angular coordinate, ϕ , represents the toroidal direction. The boundary conditions for the magnetic flux coordinate, $\psi = \psi(R, Z)$, define the poloidal boundaries, and the pressure, $p(\psi)$, and toroidal field function, $F(\psi)$, are defined as inputs. For our purposes, the “pressure factor,” $P_f \leq 1$ is utilized to modify the calculated equilibrium by artificially reducing the pressure gradient. This reduces the Shafranov shift and increases the safety factor and shear profiles by increasing the relative significance of the FF' term. This factor was

introduced to match with the original benchmarking paper, Ref. 31. This paper used a circular modified equilibrium without the Shafranov shift, so for fair comparison, we were obliged to adapt to this situation, calculating first our equilibrium and the corresponding mesh by utilizing realistic and comparable values for the current profile, but imposing an artificially reduced pressure profile. It would be possible to achieve the same result through careful and significant modification of the current profile, however, this methodology was not pursued in depth, although several results which employed this method will be discussed below.

For the duration of this paper, we use the same magnetic boundary conditions, and input profiles, and we vary only the value of P_f . This leaves the η_i profile as a function of ψ or the minor radius, r , as well as the gradients as a function of ψ unchanged. The gradients do change slightly with respect to r due to variation of the Shafranov shift with different values of P_f and the subsequent differences between the Low and High Field Sides (LFS and HFS, respectively). For this reason, all results will be reported with respect to ψ . The input profiles are based on the well-known CYCLONE base case,³¹ where we matched their values of $L_T = 25$ cm and $\hat{s} = 0.78$ where our modes are formed. A plot of the η_i parameter, along with the magnetic shear for three select values of $P_f = 1, 1/2, 1/100$, is shown in Fig. 3. These three values of shear will be used throughout the paper, and will be referred to as the *low*, *medium*, and *high shear cases*, respectively. The value of q where the modes are typically formed for these three cases are $q = 1.1, 1.25$, and 1.6 , respectively. The profiles of temperature, density, and FF' are taken as

$$T(\psi) = \left[0.0906 \tanh \left(\frac{\psi - 0.32}{0.3} \right) + 0.03 \right] \frac{1}{k_B \mu_0 n_0}, \quad (29)$$

$$\rho(\psi) = \left[0.5 \tanh \left(\frac{\psi - 0.32}{0.5} \right) + 0.5 \right] 2m_i n_0, \quad (30)$$

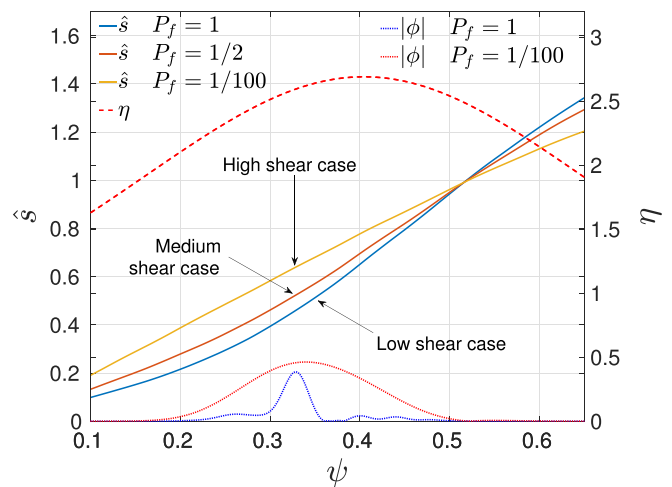


FIG. 3. Shear profile for the low ($P_f=1$), medium ($P_f=1/2$), and high ($P_f=1/100$) shear cases, alongside the η_i profile used for all simulations. Also shown are typical global profiles of ϕ identifying where the mode is commonly located.

$$FF'(\psi) = \left[3.6(1 - 1.8\psi + \psi^2) + \frac{1}{2} \operatorname{sech}^2(\psi - 10) \right] \times \left[\frac{1}{2} - \frac{1}{2} \tanh\left(\frac{\psi - 5}{0.03}\right) \right] \frac{1}{\mu_0^2}, \quad (31)$$

where ψ is normalized between 0 and 1, and $n_0 = 6.1 \times 10^{-19} \text{ m}^{-3}$. The input $p(\psi)$ is simply the product of (29) and (30). Normalizations are discussed in Sec. III B, and for the present investigation the equilibrium electrostatic potential is set to zero. In this paper, all our simulations are conducted in circular geometry with a minor radius $a = 62.5 \text{ cm}$ and a major radius $R_0 = 170 \text{ cm}$.

B. ITG model implemented in the JOREK code

For the simulation in JOREK, we adapt the system of equations for the local ITG system, defined by (2) and (21)–(23). The JOREK model includes the tITG and sITG, and also includes parallel ion motion in the convective derivatives. In addition, we retain the density convection by the ion inertial drift, $\mathbf{v}_{li} \cdot \nabla n_i$, therefore forgoing the Boussinesq approximation.⁵⁶ This is achieved by retaining the total n_i within the divergence of the (poloidal) vorticity term

$$\Omega = \nabla \cdot \left(\frac{n_i m_i}{e B^2} \nabla_{\perp} \phi \right). \quad (32)$$

Utilizing the gyroviscous cancellation,⁴⁷ with the convective derivative defined as $d/dt = \partial/\partial t + (\mathbf{v}_E + \mathbf{v}_{pi} + \mathbf{v}_{i||} \hat{\mathbf{b}}) \cdot \nabla$ in $\mathbf{v}_{li} = \omega_{ci}^{-1} \hat{\mathbf{b}} \times d\mathbf{v}_E/dt$, the inertial term becomes $\nabla \cdot (n_i \mathbf{v}_{li}) = -d\Omega/dt$. Thus, the density, pressure, and parallel velocity equations used for the simulation are⁵³

$$\frac{d}{dt} (n_i - \Omega) + n_i \nabla \cdot (\mathbf{v}_E + \mathbf{v}_{pi} + \mathbf{v}_{i||} \hat{\mathbf{b}}) = \nabla \cdot (D_{\perp} \nabla n_i), \quad (33)$$

$$\begin{aligned} \frac{d_1 p_i}{dt} + \frac{5}{3} p_i \nabla \cdot (\mathbf{v}_E + \mathbf{v}_{pi} + \mathbf{v}_{i||} \hat{\mathbf{b}}) \\ = -\frac{2}{3} \nabla \cdot \mathbf{q}^{(0)} + \nabla \cdot (K_{\perp} \nabla_{\perp} T_i + \hat{\mathbf{b}} K_{||} \nabla_{||} T_i), \end{aligned} \quad (34)$$

$$n_i \frac{d_1 v_{i||}}{dt} = -en_i \nabla_{||} \phi - \nabla_{||} p_i + \mu_{||} \nabla^2 v_{i||}, \quad (35)$$

where D_{\perp} , K_{\perp} , and $\mu_{||}$ are small diffusion coefficients used to help maintain numerical stability, and $K_{||}$ is used to encapsulate parallel temperature flux. The convective derivative in the latter two equations is $d_1/dt = \partial/\partial t + (\mathbf{v}_E + \mathbf{v}_{i||} \hat{\mathbf{b}}) \cdot \nabla$. As before, the electron dynamics is adiabatic, and the governing equation is left in the form of (1).

As with the Grad–Shafranov equilibrium, equations simulated in JOREK must be represented in cylindrical coordinates, with R and Z being the radial and vertical coordinates in the poloidal plane, and φ being the toroidal coordinate. Normalizations are chosen to leave the spatial coordinates in meters, and the time, $t \rightarrow \sqrt{\rho_0 \mu_0} t$ ($\rho_0 = 2m_i n_0$, with $n_0 = 6.1 \times 10^{-19} \text{ m}^{-3}$ being the centerline density), in units related to the Alfvén time. The magnetic field is represented as $\mathbf{B} = F_0 \nabla \varphi + \nabla \psi \times \nabla \varphi$, where $F_0 = R B_{\varphi}$, and ψ is the fixed flux function, calculated via the Grad–Shafranov equation (28). Important normalizations are $v_{i||} \rightarrow (|\mathbf{B}|/\sqrt{\rho_0 \mu_0}) v'_{i||}$, $\mathbf{v}_{(\perp)i} \rightarrow \mathbf{v}'_{(\perp)i}/\sqrt{\rho_0 \mu_0}$ (for $\mathbf{v}_{(\perp)i} \in \mathbf{v}_E, \mathbf{v}_{pi}$), $n_i \rightarrow n_0 n'_i$, $\phi \rightarrow (\tau_{IC} F_0/\sqrt{\rho_0 \mu_0}) \phi'$ (where $\tau_{IC} = m_i/eF_0\sqrt{\rho_0 \mu_0}$ is known as the diamagnetic parameter), $p_i \rightarrow p'_i/\mu_0$, $\Omega \rightarrow n_0 \Omega'$, and $T_i \rightarrow T'_i/e\mu_0 n_0$. With these normalizations

(dropping the $'$), and using $\{\cdot, \cdot\} = (\partial \cdot / \partial R)(\partial \cdot / \partial Z) - (\partial \cdot / \partial Z)(\partial \cdot / \partial R)$ as the Poisson bracket, the system of equations defined by (1), and (32)–(35) becomes

$$0 = -\frac{\tau_{IC} F_0}{R^2} n_i \frac{\partial \phi}{\partial \varphi} - \frac{\tau_{IC}}{R} n_i \{\phi, \psi\} + \tau_{IC} T_{e0} \frac{F_0}{R^2} \frac{\partial n_i}{\partial \varphi} + \tau_{IC} \frac{T_{e0}}{R} \{n_i, \psi\}, \quad (36)$$

$$\begin{aligned} \frac{\partial (n_i - \Omega)}{\partial t} = & -\tau_{IC} R \{\phi, n_i - \Omega\} + \tau_{IC} \frac{R}{n_i} \{p_i, \Omega\} \\ & - \frac{F_0}{R^2} v_{i||} \frac{\partial (n_i - \Omega)}{\partial \varphi} - \frac{1}{R} v_{i||} \{n_i - \Omega, \psi\} \\ & + 2\tau_{IC} n_i \frac{\partial \phi}{\partial Z} + 2\tau_{IC} \frac{\partial p_i}{\partial Z} - \frac{F_0}{R^2} n_i \frac{\partial v_{i||}}{\partial \varphi} \\ & - \frac{1}{R} n_i \{v_{i||}, \psi\} + \nabla \cdot (D_{\perp} \nabla n_i) - \mu_{\Omega} \nabla_{\perp}^2 \Omega, \end{aligned} \quad (37)$$

$$\begin{aligned} \frac{\partial p_i}{\partial t} = & -\tau_{IC} R \{\phi, p_i\} - \frac{F_0}{R^2} v_{i||} \frac{\partial p_i}{\partial \varphi} - \frac{1}{R} v_{i||} \{p_i, \psi\} \\ & + 2\gamma \tau_{IC} p_i \frac{\partial \phi}{\partial Z} + 2\gamma \tau_{IC} T_i \frac{\partial p_i}{\partial Z} - \gamma \frac{F_0}{R^2} p_i \frac{\partial v_{i||}}{\partial \varphi} \\ & - \gamma \frac{1}{R} p_i \{v_{i||}, \psi\} + 2\gamma \tau_{IC} p_i \frac{\partial T_i}{\partial Z} \\ & + \nabla \cdot (K_{\perp} \nabla_{\perp} T_i + \hat{\mathbf{b}} K_{||} \nabla_{||} T_i), \end{aligned} \quad (38)$$

$$\begin{aligned} B n_i \frac{\partial v_{i||}}{\partial t} = & -B n_i \tau_{IC} R \{\phi, v_{i||}\} - B n_i \frac{F_0}{R^2} v_{i||} \frac{\partial v_{i||}}{\partial \varphi} \\ & - \frac{B n_i}{R} v_{i||} \{v_{i||}, \psi\} - \frac{F_0}{R^2} n_i \frac{\partial \phi}{\partial \varphi} - \frac{1}{R} n_i \{\phi, \psi\} \\ & - \frac{F_0}{R^2} \frac{\partial p_i}{\partial \varphi} - \frac{1}{R} \{p_i, \psi\} + B \mu_{||} \nabla^2 v_{i||}, \end{aligned} \quad (39)$$

respectively, where

$$\Omega = \tau_{IC}^2 \nabla \cdot (n_i R^2 \nabla_{\perp} \phi), \quad (40)$$

and $p_i = n_i T_i$ represents the pressure.

For the duration of our analysis, we use $F_0 = 3.247 \text{ T m}$, and unless otherwise specified, we use the value of $\tau_{IC} = 0.01 \text{ T}^{-1}$. Our diffusivities are maintained at or near $D_{\perp} = K_{\perp} = \mu_{||} = 2.5 \times 10^{-5} \text{ T m}$ and $K_{||} = 0.1 \text{ T m}$.

JOREK uses Fourier decomposition (in the toroidal harmonic, n) to solve these equations in the toroidal direction. In all of our current simulations, we omit the evolution of the $n=0$ harmonic, which means that the equilibrium is fixed. A large portion of the analysis presented in this paper is concerned with the behavior of single- n modes. We will refer to these simulations as linear, although a range of m harmonics will still be stimulated, and will indeed interact with each other (through cubic coupling discussed in Sec. VII A) when the perturbations reach significant amplitudes.

IV. LINEAR BENCHMARKING

To validate our model, we compare the linear growth rates of our simulations to the CYCLONE base case.³¹ We use the high shear equilibrium, which has a linear shear profile (see Fig. 3), and parameters which are the closest to that in Ref. 31. The majority of the results in

that paper were completed in flux-tube geometry, and are linear in both n and m , whereas our simulations are linear only in n , and allow a spectrum of m to be excited over the full range of rational surfaces. Thus, to compare our results, we Fourier decompose each (individually simulated) toroidal mode, n , into its constituent poloidal harmonics, and report the growth rate of the largest amplitude poloidal harmonic, m , converted into units of $k_\theta \rho_i$ (k_θ is equivalent to k_y in the local model) to maintain the same axes as in Ref. 31.

The data in Ref. 31 was collected using an $s - \alpha$ equilibrium model,⁵⁴ where the magnetic shear, s , and the Shafranov shift, α , are used to define the equilibrium. Furthermore, to compare with the previously published results, the authors in Ref. 31 set the Shafranov shift to zero. For comparison with Ref. 31, we artificially reduced the Shafranov shift, by utilizing $P_f = 1/100$, and matched their value of $\hat{s} = 0.78$ at the location of our maximum temperature gradient. The growth rate and frequency data from our benchmarking simulations are shown in Fig. 4, along with the data from Ref. 31, and our analytical results for the linear ITG model (2) and (13)–(15). Although we artificially reduced the Shafranov shift, we still found discrepancies to the Ref. 31 data, however, this originates from specific differences with the $s - \alpha$ equilibrium model, as reported in Ref. 32. In that paper, simulations performed using an $s - \alpha$ equilibrium with a zero Shafranov shift, as in Ref. 31, were shown to possess a reduced growth rate in comparison to those calculated using a Grad–Shafranov MHD, or circular-concentric equilibrium. Thus, our data agrees quite well with the circular-concentric results in Ref. 32, which is comparable to our reduced Shafranov shift (high shear case) results.

V. EIGENMODE STRUCTURE FOR LOW AND HIGH SHEAR

In varying the magnetic shear, we noticed the development of two drastically different eigenmode structures. These will be referred to as the *ballooning* and *localized* mode structures. The ballooning

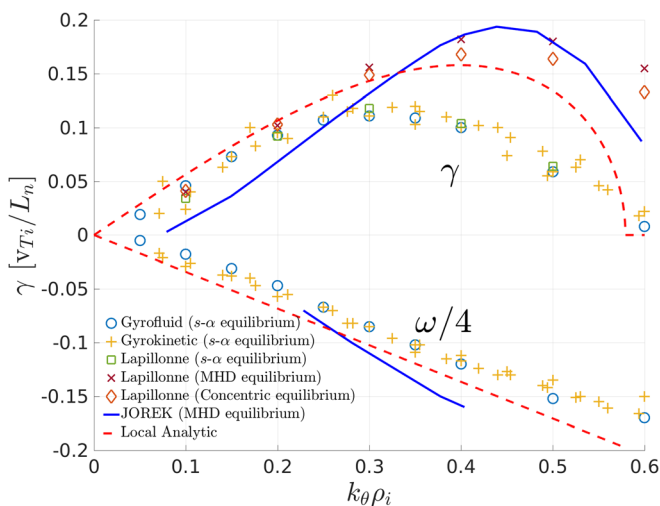


FIG. 4. Growth rate and frequency of ITG modes in JOREK and the local model, compared to the standard CYCLONE case³¹ (“Gyrofluid” and “Gyrokinetic” data points), and the results in Ref. 32 (“Lapillonne” data points). Normalized with $v_{Ti} = 4.48 \times 10^5$ m/s and $L_n = 76.6$ cm.

structure [Fig. 5(b)] consists of radially elongated vortices which span a large number of rational surfaces. In contrast, the localized mode structure [Fig. 5(a)] consists of a radially narrow band of vortices, localized near a particular rational surface, and exhibiting a larger poloidal than radial extent. Multiple bands of the localized mode structure can occur in the same simulation, near different rational surfaces, as shown in Fig. 6, and there can additionally be *mixed states* consisting of both localized and ballooning mode structures, as shown in Fig. 7 [and later in Fig. 22(a), where the ballooning mode has a larger relative amplitude]. All of these modes rotate clockwise, in the ion diamagnetic direction, and in all of the poloidal cross sections, the HFS is on the left.

The characteristic features of the mode structures described here are the consequence of global toroidal geometry and realistic toroidal equilibrium which provides specific coupling of the ITG eigenmodes localized on the corresponding rational surfaces. The characteristics of other high- n ballooning modes may vary for different types of modes, e.g., drift waves, resistive instabilities, and interchange modes. Although similar phenomena may arise in other models, we consider only the specific case of ITG eigenmodes here.

The ballooning mode structure is formed when there is strong coupling between neighboring rational surfaces. This is facilitated by reducing the distance between rational surfaces, $\Delta = 1/nq' = r/nq\hat{s}$. Thus, at a given radius, increasing the magnetic shear, safety factor, and toroidal mode number all tend to increase the likelihood of forming a ballooning mode structure. We find that when $P_f \leq 1/2$, corresponding to the medium and high shear cases, which also possess a higher q -profile, almost all simulations favor the ballooning mode structure. The only exceptions are at mode numbers $n \leq 20$ which present mixed states, or localized modes which occur at the lowest unstable n for each level of magnetic shear. For the low magnetic shear case (see Fig. 3), mixed states are most common, with purely localized mode structures occurring for $n \leq 20$. This breakdown of the ballooning structure at low shear has been predicted in previous papers, with some authors predicting the formation of Fourier modes,⁵⁵ and others predicting the formation of so-called infernal modes.^{56–58} Our localized mode may be an incarnation of the infernal modes since they favor lower n and m , and appear in bands, however, the theory in Ref. 56 predicts complete (ballooning) stability before the onset of infernal modes, only at very low n , whereas we see the development of mixed modes for intermediate n 's. We should also note that the breakdown of ballooning modes into radially localized mode structures has also been found when including flow shear.⁵⁹

The difference in the amplitude of the localized mode from the HFS to the LFS is not as pronounced, which is characteristic of the sITG (unstable on both the HFS and LFS). As the shear is increased, the sITG is stabilized (as discussed at the end of Sec. II C), allowing more tITG effects to come into play. Although in the local model, the overall ITG behavior is also stabilized at higher shear, an additional (global) factor comes into play once the ballooning mode is formed. Ballooning modes profit from the constructive interference of different modes on different rational surfaces. On the LFS, the (cos and sin) wave peaks which constitute the base-level structure of the modes on each rational surface are aligned; this coupling allows global ballooning modes to retain instability even when the individual harmonics are stable (a good description of this effect is available in Ref. 60).

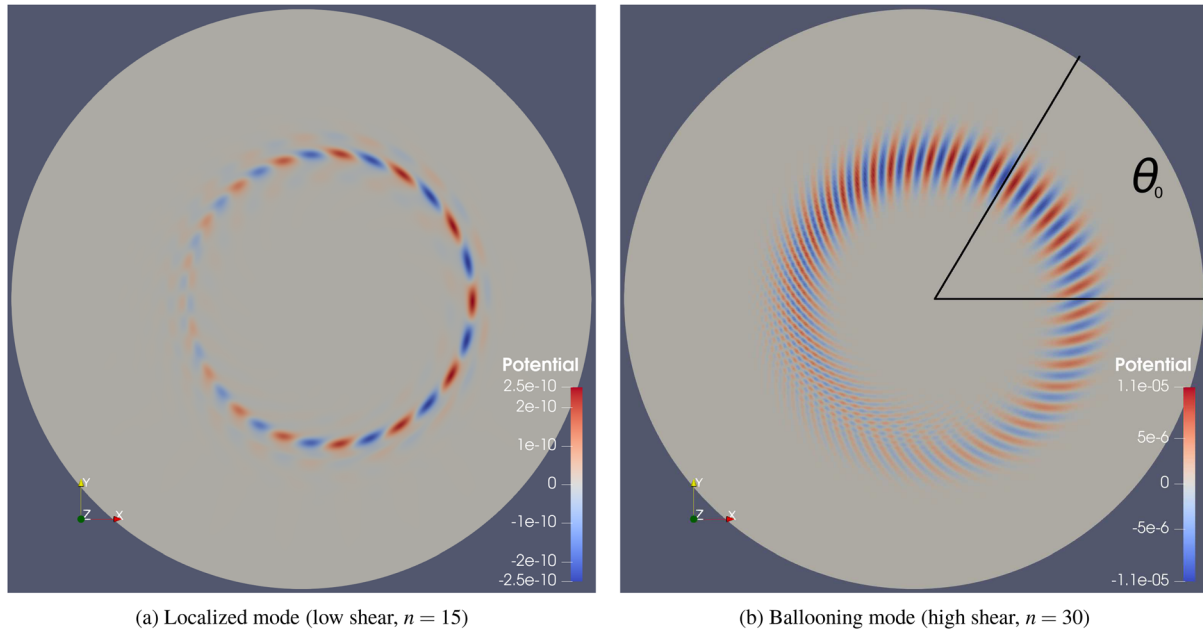


FIG. 5. Poloidal cross section of potential, ϕ , for the localized (a) and ballooning (b) modes.

A. Localized mode structure

The localized mode, shown in Fig. 5(a), is the simplest structure formed in our simulations. Localized modes are symmetric about the midplane, $\theta = 0$, and exhibit a larger poloidal than radial extent.

A poloidal Fourier decomposition of the two localized mode structures in Fig. 6 is shown in Fig. 8. The two peaks between $\psi = 0.3$ and 0.35 constitute the inner localized mode, and the two peaks between $\psi = 0.35$ and 0.4 constitute the outer mode. Considering the data points, it can be seen that the localized mode is formed by two

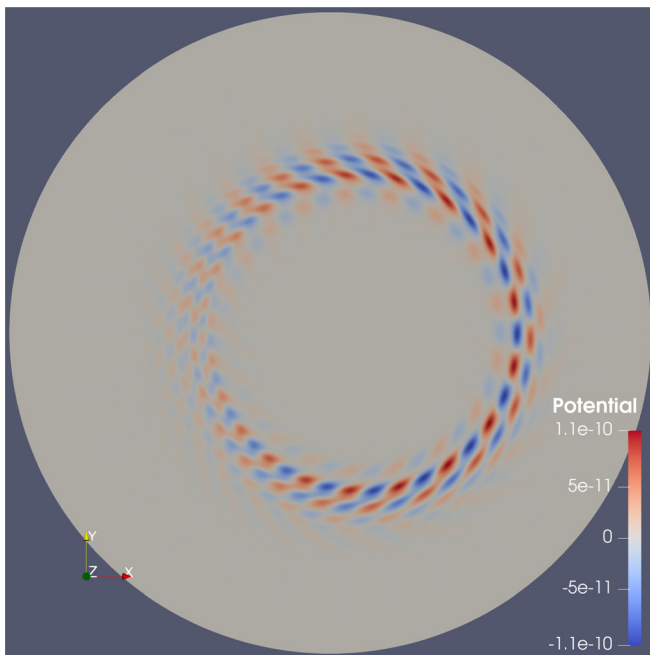


FIG. 6. Poloidal cross section of ϕ showing two coexisting localized modes (low shear, $n = 20$).

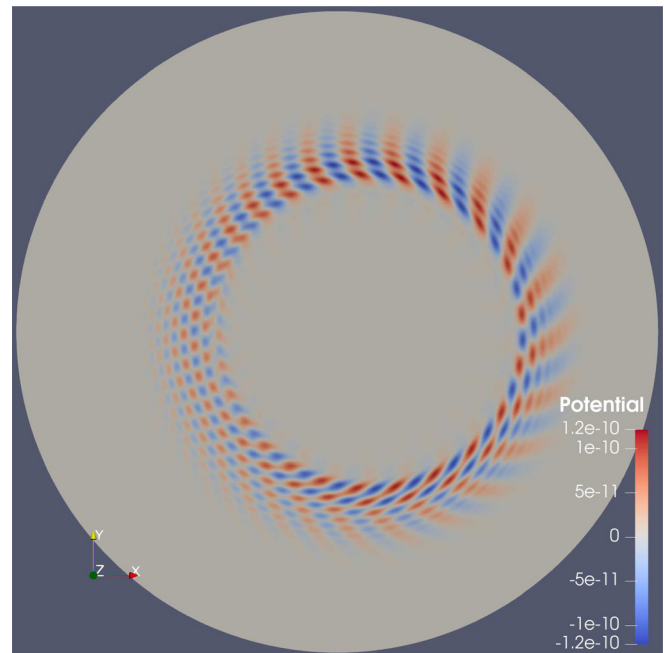


FIG. 7. Poloidal cross section of ϕ showing a mixed state (low shear, $n = 25$).

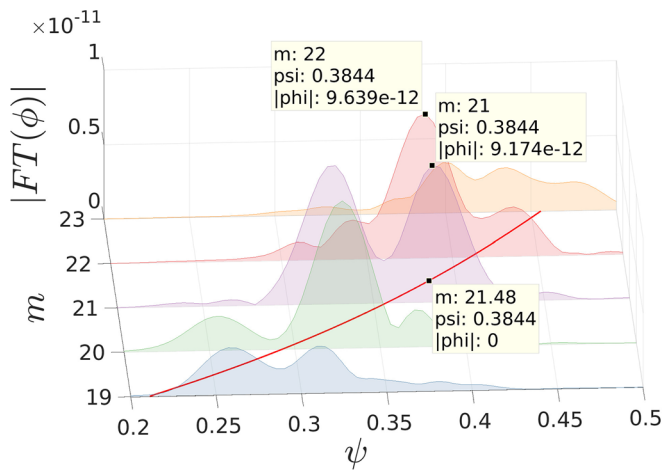


FIG. 8. Poloidal Fourier decomposition of ϕ for the two localized mode structures in Fig. 6 (low shear, $n=20$), along with a red line showing the location of $m = q(\psi)n$. Data points identify that the two peaks at $\psi = 0.3844$ occur where $m = 21.48$ based on the q -profile.

peaks in Fourier amplitude originating from two adjacent rational surfaces, but overlapping precisely (in both the radial location and amplitude) between the corresponding rational surfaces. The width of these Fourier peaks spans only the distance between the two involved rational surfaces, and the Fourier amplitude goes nearly to zero on the rational surfaces. For multiple adjacent localized modes, as in Fig. 6, the rational surface between localized modes is involved in both neighboring structures, exhibiting a double Fourier peak ($m = 21$ in Fig. 8). When the real and imaginary components of the Fourier transform are considered, the two peaks of the middle Fourier harmonic have opposite polarity, highlighting that the magnitude goes to zero on the rational surface.

The global profile of the localized mode is shown in the second plot in Fig. 9, along with vertical lines identifying rational surfaces at $m = 14 : 20$ and $n = 15$. The η_i profile is also shown in the first plot of Fig. 9. Here, as well, it is clear that the mode is localized directly between the rational surfaces, and we find that the localized modes always form at radii slightly below the peak in η_i . This is because the localized mode favors instability at a lower m , where the spacing between rational surfaces is larger.

B. Ballooning mode structure

The ballooning mode structure [Fig. 5(b)], presents vortices which are formed in an up-down asymmetric fashion—the most radially symmetric vortex is formed above the outboard midplane. This rotation from the outboard midplane is commonly enumerated by the ballooning angle, θ_0 . A finite ballooning angle can arise in global simulations due to geometric asymmetry, such as the limiter position, the existence of poloidal flows, or due to higher order effects of the global profiles.^{1–3} Only the later situation is present in these simulations. This mechanism also appears in higher order ballooning theories,^{1,7} which find finite θ_0 arising due to 2D effects and second or higher order derivatives of the considered profiles. In flux tube models, θ_0 can be added as a parameter, and the maximum growth rate is found for

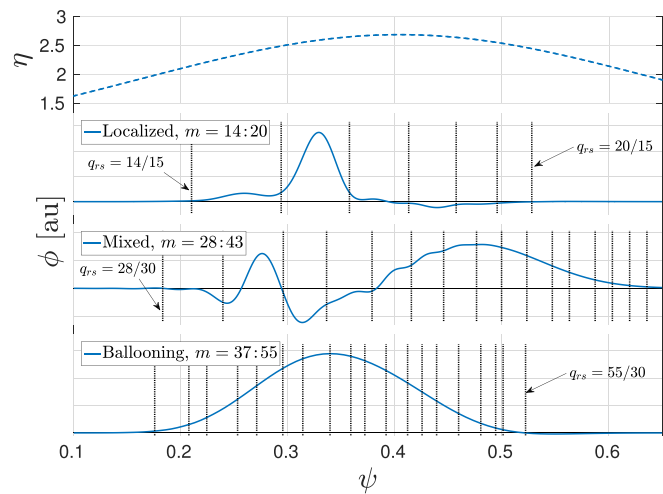


FIG. 9. Typical global profiles of ϕ along with the η profile for localized (low shear, $n = 15$), mixed (low shear, $n = 30$), and ballooning modes (high shear, $n = 30$). The vertical lines indicate rational surfaces at $q_{rs} = m/n$ with the m values shown.

$\theta_0 \neq 0$. In these theories, there is not always a distinction in the maximum growth rate for either positive or negative θ_0 .^{4,5} In our simulations, we ubiquitously found $\theta_0 > 0$, unless a negative value of τ_{TC} was used, which corresponds to a reversed direction of the diamagnetic drift.

The mechanism which leads to finite θ_0 in our simulations is similar to finite θ_0 which may arise due to poloidal flows,⁶⁰ however, it originates from the diamagnetic drift. Strong pressure gradients lead to a significant shear in the (poloidal) diamagnetic drift, and the difference in rotation velocities at different rational surfaces yields a nonuniform Doppler shift. This shifts the location where the LFS constructive interference occurs, and rotates it in a direction opposite to the direction of the diamagnetic rotation.

Considering different toroidal mode numbers, we find that the ballooning angle increases with n , as shown in Fig. 10. This increase is due to the increasing density of rational surfaces leading to enhanced toroidal coupling. There is also a significant increase in θ_0 between the high and medium shear cases, however, this is due to the mode localization. For reasons which will be discussed later in this section, the mode structure for the medium shear case appears at larger radii. This allows it to reside in a region where the gradients are stronger, causing it to have a larger ballooning angle, varying from $\theta_0 = 72^\circ$ at $n = 25$ to $\theta_0 = 103^\circ$ at $n = 55$, whereas for the high shear case, it varies from $\theta_0 = 56^\circ$ at $n = 20$ to $\theta_0 = 80^\circ$ at $n = 45$. It may be noticed that there is a slight concavity at the location of θ_0 (toward the right of the θ_0 line) in Fig. 10(a), however this is due to effects at the edge, arising from weaker coupling. The identified ballooning angle is measured directly from the magnetic axis to the most radially symmetric vortex, and includes the appropriate Shafranov shift—using a smaller value of θ_0 , where the edge effects are smaller, yielding vortices that are tilted with respect to the true radial direction.

As n is increased, there is also an increase in the prevalence of the tITG mechanism. This can be seen by the increasing stability on the HFS. Although in the local model, the sITG is stable to larger poloidal

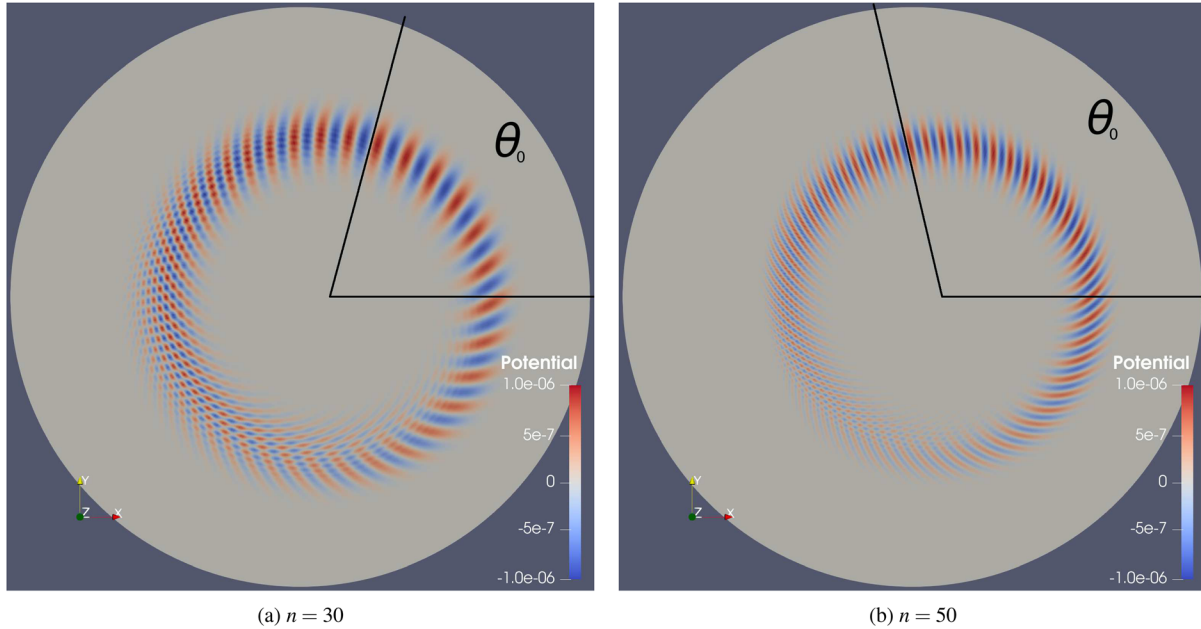


FIG. 10. Poloidal cross section of ϕ for medium shear at $n = 30$ (a) and $n = 50$ (b) showing an increase in ballooning angle with n .

mode numbers (and thus larger toroidal mode numbers, since $m = q(\psi)n$), decreasing the spacing between the rational surfaces increases the toroidal coupling which brings out more TITG effects within the ballooning mode.

A poloidal Fourier decomposition of the perturbed potential for the ballooning mode is shown in Fig. 11. The width of each Fourier peak spans several rational surfaces, identifying the strong coupling between modes, yielding the smooth, wide, mode envelope which is

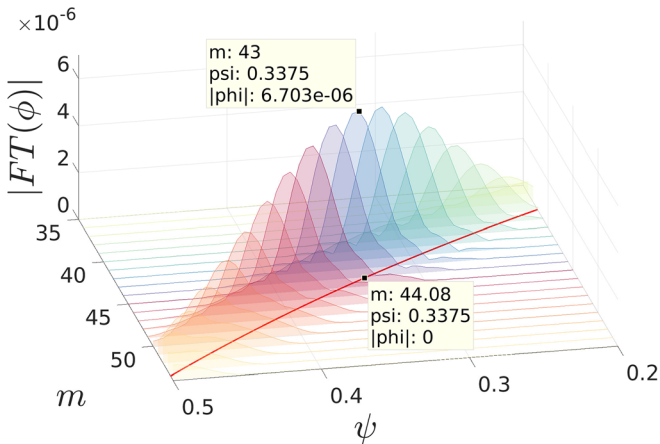


FIG. 11. Poloidal Fourier decomposition of ϕ for the high shear case in Fig. 5(b) ($n = 30$), along with a red line showing the location of $m = q(\psi)n$. Note that the nonintuitive direction of the axes is chosen for visual clarity. Data points identify that the peak for $m = 43$ at $\psi = 0.3375$ occurs where $m = 44.08$, based on the q -profile.

characteristic of ballooning modes. Contrary to expectations, the peaks in Fourier amplitude for each m harmonic are shifted to larger radii by an entire rational surface. In Fig. 11 the $m = 43$ Fourier peak occurs where $m = 44.08$ according to the q -profile. This shift from the mode's rational surface has been discussed in terms of an imaginary component to the ballooning angle,^{3,7,61–63} however to our knowledge, such large values of this shift have never been discussed.

To investigate this effect further, we performed a scan of the τ_{IC} parameter from $\tau_{IC} = 0.006$ to $\tau_{IC} = 0.021$. This was completed for the high shear case with $n = 30$, which is the same value as in Fig. 5(b), where $\tau_{IC} = 0.01$. Increasing τ_{IC} increases the relative strength of the diamagnetic effects, leading to an increased ballooning angle as shown by the difference between Figs. 12(a) and 12(b). Increased toroidal coupling can also be seen by the increasing width of the Fourier peaks between Figs. 13(a) and 13(b), along with the increasing number of poloidal harmonics involved. Observing the displayed data points in these figures, we can see that as the value of τ_{IC} is increased, the radial shift increases from 0.85 rational surfaces in Fig. 13(a), to two whole rational surfaces in Fig. 13(b)! This is far beyond what is typically expected, however it can be shown to be a possibility within the framework of higher order ballooning theory, as described in Ref. 7. In Ref. 7, Eq. (104) shows that the imaginary component of the ballooning angle, η_0 , which identifies the radial shift of the mode location, can be written as

$$\eta_0 = -\frac{1}{2} \frac{\hat{s} - 1}{\left(\hat{s} - \frac{1}{2}\right) - \frac{\omega}{\omega_{Di}} k_{\theta}^2 \rho_i^2 \hat{s}^2} \theta_0. \quad (41)$$

This identifies that the shift from the rational surface is directly proportional to the ballooning angle, and is dependent on the magnetic

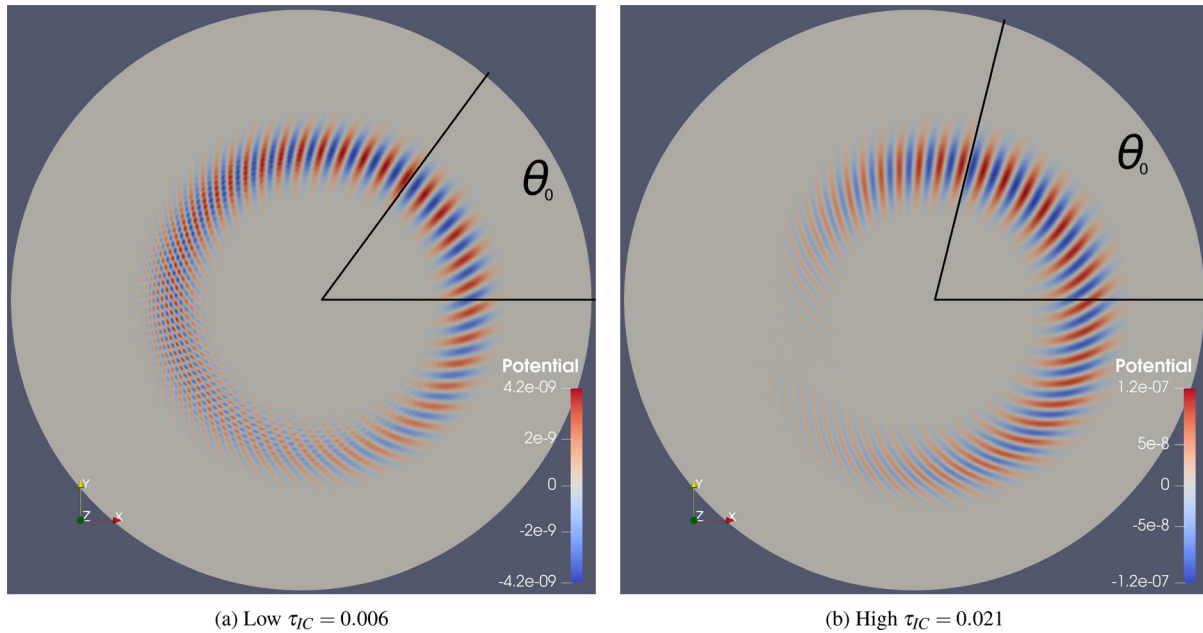


FIG. 12. Poloidal cross section of ϕ for low (a) and high (b) τ_{IC} (high shear, $n = 30$).

shear, which agrees well with our results. It can be seen, however, that for particular values of $(\omega/\omega_{Di})k_{\theta}^2\rho_i^2$, this equation experiences a singularity. Although our value of $(\omega/\omega_{Di})k_{\theta}^2\rho_i^2$ is typically near this singularity (resulting in moderately large values of η_0/θ_0 , between 0.7 and 1.5), our shift results are far less variable than this function near its singularity. Even when the ballooning mode arises as part of the mixed mode [Figs. 7 and 22(a)], where it is somewhat disfigured and rotates with a significantly reduced ω (as will be discussed in Sec. VC), the shift is still around one rational surface [Figs. 14 and 22(b)] as is the case for all of our results with $\tau_{IC} = 0.01$.

Furthermore, there should be qualitative changes (due to the sign changes) when \hat{s} is on either side of 1, or when $\theta_0 < 0$ (which occurs

for a negative τ_{IC} , and also negates both ω and ω_{Di}) which we do not observe—our shift is always outwards, toward larger rational surfaces. In every single simulation which develops a ballooning-type structure, we witness this shift, and the amplitude of the mode on the corresponding rational surface is usually quite small, typically being less than 1/3 of the peak amplitude, and often being much less. Since the ballooning modes only arise when we utilize the factor P_f there may be some concern that this shift is associated with this artificial modification of the equilibrium. We have concluded that this is not the case, however, as in studies where we achieved the ballooning structure through significant modification of the current profile (using $P_f = 1$), we witnessed similar values for the radial shift, varying from 0.5 to 1.4

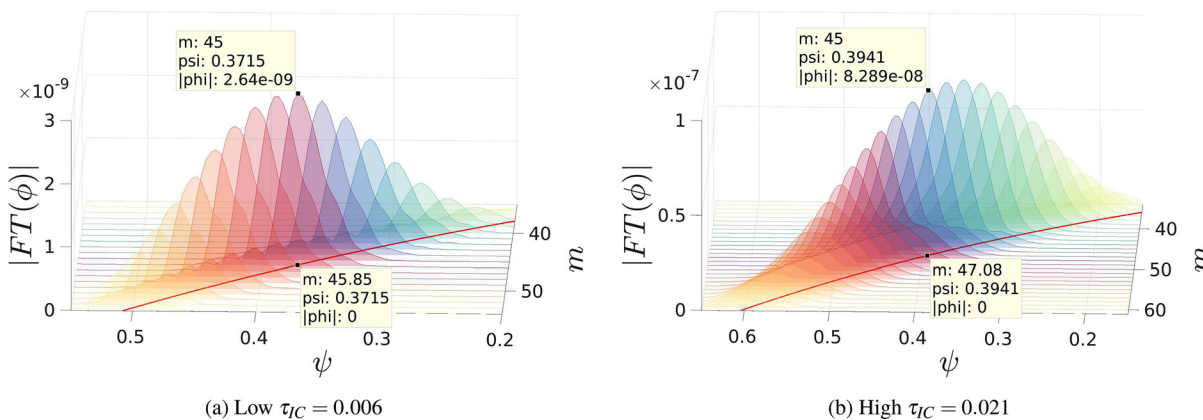


FIG. 13. Poloidal Fourier decomposition of ϕ for low (a) and high (b) τ_{IC} cases in Fig. 12 (high shear, $n = 30$), along with a red line showing the location of $m = q(\psi)n$. Note that the nonintuitive direction of the axes is chosen for visual clarity. Data points identify that for low τ_{IC} , the peak for $m = 45$ occurs at $\psi = 0.3715$, where $m = 45.85$ based on the q -profile, whereas for high τ_{IC} , it occurs at $\psi = 0.3941$, where $m = 47.08$.

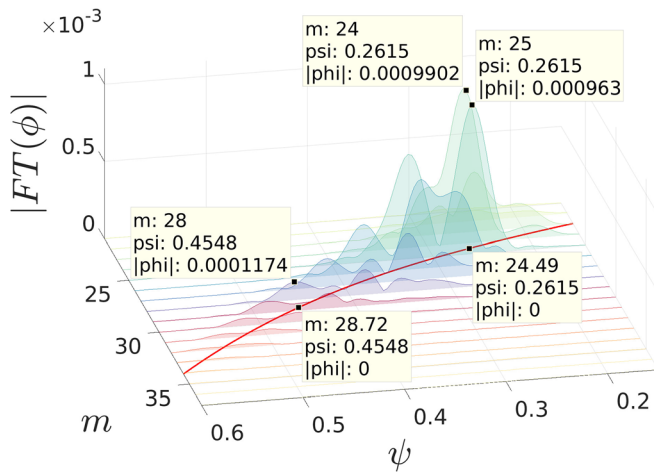


FIG. 14. Poloidal Fourier decomposition of ϕ for the mixed state in Fig. 7 (low shear, $n = 25$), along with a red line showing the location of $m = q(\psi)n$. Note that the nonintuitive direction of the axes is chosen for visual clarity. Data points identify that the localized mode peaks for $m = 24$ and 25 at $\psi = 0.2615$ occur where $m = 24.49$, based on the q -profile, whereas the $m = 28$ peak of the ballooning mode structure (still valid, although of a lower relative amplitude) at $\psi = 0.4548$ occurs where $m = 28.72$.

rational surfaces. Furthermore, the strong dependence of this shift on parameters such as τ_{IC} identify a more fundamental root.

The origin of this shift could be due to the ballooning mode being composed of localized modes, rather than simple Fourier harmonics. In the transient phase, as the modes are forming, multiple localized modes come together to form the ballooning structure. This is observed both in the evolution of the poloidal cross section and Fourier decomposition, where the dual peaks for a given m (see, e.g., $m = 21$ in Fig. 8) begin to grow at uneven rates. Since the coupling is stronger at larger radii, due to the increasing shear, the peaks which are formed at larger radii grow faster, and soon come to dwarf the peaks at smaller radii (which still grow, just at a significantly slower rate). As the ballooning mode is formed, the dual peaks also become coupled together and begin to merge. Evidence for this behavior is visible in both Fig. 13(b) where there are subtle bumps closer to the rational surface which only exist at larger radii/ m (where there are less significant-amplitude poloidal harmonics above them, and thus the coupling from below is stronger), and Figs. 14 and 22(b), where the ballooning component of the mixed mode exhibits a smaller secondary peak, closer to the rational surface. The shift of the harmonics decreases as we travel to larger radii/ m , suggesting the effect weakens as there are less harmonics above to couple to the larger radii harmonics, however, it is yet unclear why the shift is always greater than 0.5 (the outwards shift of the localized mode). These effects are exemplified in Fig. 15, which corresponds to Fig. 10(b), and shows a valley in the Fourier amplitude, formed at the rational surfaces. The large peaks of the typical ballooning structure, at high radii, are shifted by 1.5 rational surfaces outwards, and the smaller peaks, which look like remnants of the localized mode structure's double peak (e.g., $m = 21$ in Fig. 8), still remain at lower radii, shifted inwards by only 0.4 rational surfaces. Thus, we expect that the peaks are pulled to larger radii because the density of rational surfaces is higher there, and thus

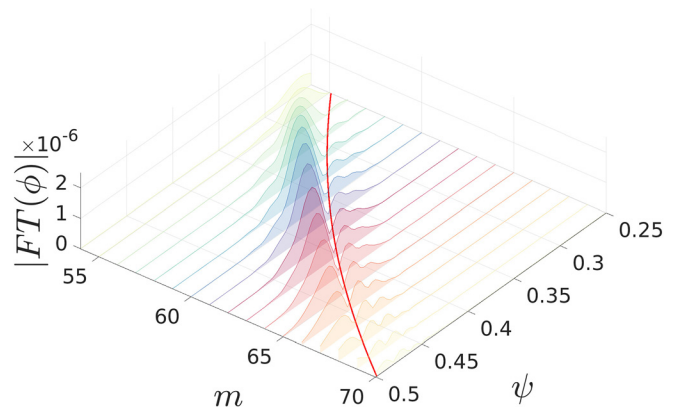


FIG. 15. Poloidal Fourier decomposition of ϕ for Fig. 10(b) (medium shear, $n = 50$), along with a red line showing the location of $m = q(\psi)n$, and a corresponding valley in the Fourier peaks. Note that the nonintuitive direction of the axes is chosen for visual clarity. The tall peaks at larger radii are shifted outwards by 1.5 rational surfaces, and the small peaks at lower radii (remnants of the second peak in the localized mode) are shifted inwards by 0.4 rational surfaces.

inverting the shear profile should lead the shift of the ballooning mode to be toward the inside of the rational surfaces. This is likely not the only effect at play, however, it presents one option as to why our simulations always witness an outward radial shift.

Another difference noticed in the scan of τ_{IC} is the variation in how the ballooning mode mixes with itself on the HFS. This mixing occurs as a result of the destructive interference which occurs on the HFS. The destructive interference originates from the difference in mode numbers on adjacent rational surfaces, which must be reconciled (since all their peaks align on the LFS, there must be destructive interference on the HFS).⁶⁰ For low τ_{IC} [Fig. 12(a)], the mode structure is symmetric about the ballooning angle, and the elongated vortices fragment into a large number of small circular vortices on the HFS. Looking closely at the Fourier transform [Fig. 13(a)], we see that there is only a significant radial overlap between m and $m + 1$ (only small portions of the tails of m and $m + 2$ coincide), thus it makes sense that the global structure would possess a poloidal mode number of 1 (symmetric about the ballooning angle). For larger values of τ_{IC} , there begins to be a significant overlap between m and $m + 2$ [Fig. 13(b)] which leads to some poloidal structure with a mode number of 2, resulting in the asymmetry of about θ_0 , which is shown in Fig. 12(b). At angles just above θ_0 , the mode behaves like for a small τ_{IC} —it becomes concave toward the ballooning angle, and tilts slightly as we move to higher θ . For angles smaller than the ballooning angle, however, the inclination of the mode is much more severe, and by the time we consider $\theta = \theta_0 - 180^\circ$, the vortex is nearly aligned with the poloidal direction. When the mode mixes with itself on the HFS, the lower leg of the mode wraps around the outside of the upper leg. Looking closely at the difference between Figs. 10(a) and 10(b), we see that this behavior is also witnessed for higher toroidal mode numbers. Higher n also experience broadening Fourier peaks which overlap more, along with the involvement of more poloidal harmonics and larger shifts from the rational surfaces. Thus, for all results with either a decreased spacing between rational surfaces, or increased diamagnetic effects, we see increasing overlap between the Fourier peaks, and an increasing

number of Fourier peaks involved, leading to a larger ballooning angle and larger shift off of the rational surface.

Finally, the mode amplitude at low τ_{IC} [Fig. 12(a)] remains relatively consistent from the LFS to HFS, which is indicative of the instability being dominated by the sITG (which is still unstable on the HFS). As the diamagnetic (and thus toroidal) effects are increased, the difference between HFS and LFS becomes more distinct [Fig. 12(b)], thus associating the ballooning angle with tITG effects.

We now move on to the radial structure of the global ballooning mode and mixed mode, which are shown earlier in Fig. 9, along with the rational surfaces present, and the η_i profile. Of course, since the radial structure of the ballooning mode is sensitive to the sampling angle θ , we take the radial profile at the ballooning angle, $\theta_0 = 60^\circ$.

The radial location at which each mode structure is centered is mainly a function of the most unstable poloidal harmonic, m , for that mode structure. Thus, for the medium shear case, the ballooning modes are formed at a notably higher radius since the most unstable m harmonic for the ballooning mode (at that n) occurs there [observe the difference between Figs. 5(b) and 10(a)]. This behavior is visible for the mixed mode in Fig. 9, which is shown here for low shear, and thus the ballooning structure occurs at quite a large radius. The localized components of the mixed modes are also located between the rational surfaces, however, there is some interaction between the localized modes which pulls the modes outward slightly, adding evidence to our observation that the shift of the ballooning harmonics off of the rational surfaces, comes from the interaction of localized mode harmonics. Of course, the radial shift of the ballooning mode Fourier harmonics also appears in the global mode, as well. Thus, for the pure-ballooning mode in Fig. 9, although the maximum amplitude Fourier harmonic is $m = 43$ (Fig. 11), the global mode peak appears much closer to the rational surface $q_{rs} = 44/30$.

C. Growth rate and frequency of localized and ballooning modes

A summary of the growth rates at the three considered levels of magnetic shear is shown in Fig. 16. Here, we see that increasing the magnetic shear leads to faster growing modes. These higher shear simulations strongly favor the ballooning structure, as discussed at the beginning of Sec. V. Although our independent variable is n , we find the stability to rely mostly on the poloidal harmonic. Thus, if the growth rate is plotted with respect to m , the left- and right-hand sides of the growth rate curves overlap, and it is just the peaks that are higher, with the most unstable m always being around $m = 43$. Increasing the magnetic shear brings the rational surfaces together and increases the constructive interference. Increased shear was, however, attained by decreasing the factor P_f [see Eq. (28) and Fig. 3], which also reduces the Shafranov shift. This can further destabilize the mode, since for a reduced Shafranov shift, the mode spends more of its rotation on the LFS, in the unfavorable curvature region.⁶⁰

As mentioned earlier, for a positive τ_{IC} , all of the modes rotate clockwise in the ion diamagnetic direction. To measure this rotation, we take a cross section of the potential along the minor radius at the ballooning angle and study the particular radial location(s) where the mode amplitude is the maximum (multiple locations for multiple concurrent mode structures). We then Fourier transform the time evolution of the potential at these points to identify the mode frequency—

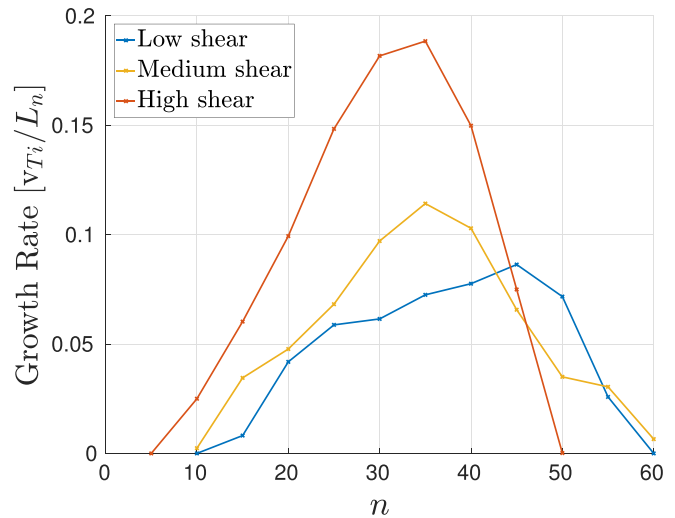


FIG. 16. Growth rates of the ITG mode as a function of toroidal harmonic for the low, medium, and high shear cases. Normalized with $v_{Ti} = 4.48 \times 10^5$ m/s and $L_n = 76.6$ cm.

since the speed of mode rotation is consistent at all poloidal angles, this frequency characterizes the mode rotation.

For high shear, essentially all simulations of different toroidal harmonics form the ballooning mode structure. This structure possesses a single, consistent, mode frequency, and can be identified by its largest amplitude poloidal harmonic, m . Conversely, for low shear, a wide variety of mode structures are formed, each with their own frequency, and dominant poloidal harmonic, m . To show these frequencies together, we plot them against the dominant poloidal harmonic for each structure, such that for a single n , the multiple structures formed in a single low shear simulation can be shown. This is done in Fig. 17, where circular points represent the ballooning structure, and x's represent the localized structure. The high shear case is plotted in magenta, and the dotted line then connects multiple simulations at different n , each which forms a single ballooning structure with a single dominant poloidal harmonic, m . For low shear simulations, each simulation is plotted with its own color, and a solid line connects different structures occurring in a single simulation.

To become familiar with this plot, consider the high shear case, where magenta circles represent the resultant ballooning modes. As we traverse from the bottom left, along the dotted line, we begin with $n = 15$ and progress by 5 to $n = 45$. For the low shear case, we begin with $n = 15$, also in the bottom left, which forms a single localized mode, shown with a blue x. To consider simulations at increasing n , we then traverse between the different sets of colored points. Individual simulations which form mixed states are connected by the solid lines, where the structures with lower m occur at smaller radii and have larger frequencies.

Based on the local model, the mode frequency should increase significantly with increasing magnetic shear. Although, for a given n , Fig. 17 shows that the frequency of the high shear case is typically greater than that of the low shear case, the difference is not that substantial. Furthermore, focusing on the low shear case, the increase in frequency for the localized mode structures (x's) follows a different

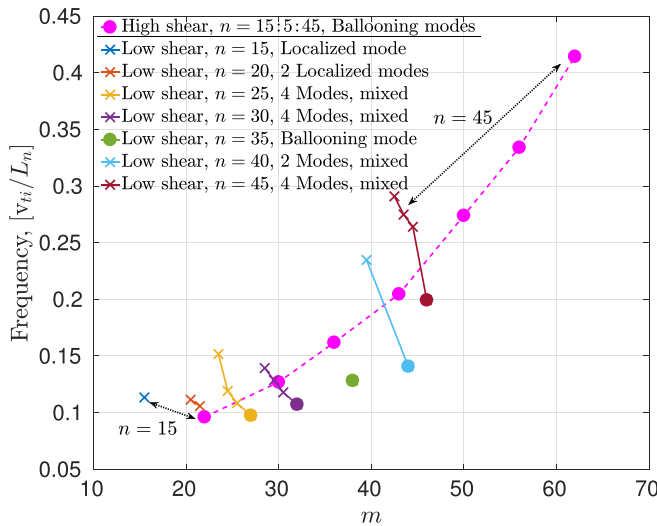


FIG. 17. Mode frequencies for both low and high shear cases. Each n of the high shear case yields a ballooning mode, with a single dominant m and frequency (magenta). For low shear, most simulations form mixed states composed of multiple structures, where each structure has its own dominant m and frequency. In this case, each simulation has its own color, and the structures within it (points) are connected by a solid line. Localized structures are x's and ballooning structures are circles.

trend than the ballooning modes (circles), appearing in the same simulation. For the mixed states, the (inner) localized modes can rotate with a vastly larger frequency than their neighboring ballooning mode. When only the ballooning structure is formed, as is the case for $n = 35$, the frequency follows the trend of the other ballooning modes. These factors serve to identify that the mechanism behind the mode rotation is different for the localized and ballooning modes. For the (disconnected) localized modes, the frequency is like that for the local model, namely a consequence of the mode itself. For the ballooning mode on the other hand, the rotation frequency is governed by the strong coupling between the constituent Fourier modes. This is what causes the frequency of the ballooning structures in the mixed mode to be so much lower than that of the coexisting localized modes, and leads the purely ballooning mode simulations at high shear to exhibit a relatively small increase in the mode frequency overall, compared to the low shear cases.

VI. REYNOLDS STRESS

As mentioned in Sec. I, a key term in the development of shear and zonal flows is the Reynolds stress, which is typically represented as $\bar{\mathbf{R}} = \langle \mathbf{v} \otimes \mathbf{v} \rangle$. It is most common to consider the Reynolds stress generated by the $E \times B$ velocity alone, which is what we will use in the upcoming analysis. The Reynolds stress is a ponderomotive effect (i.e., originating from a quadratic combination of a single variable) of flow velocity, and its flux is what provides the drive of momentum transport in the momentum equation: $\partial \mathbf{v} / \partial t + \nabla \cdot \bar{\mathbf{R}} = -\nabla p / \rho + \dots$. It is most common to study the $n = m = 0$ component of the Reynolds stress, due to its ability to generate zonal flows, however, other components of the Reynolds stress may be implicated in the development of GAMs⁶⁴ ($n = 0, m = 1$), and other finite mode number phenomena.³⁴

In our model, the Reynolds stress appears in the ion continuity equation (33) or (37) via the generalized vorticity term Ω . The term we measure is

$$S = \mathbf{v}_E \cdot \nabla \Omega = \hat{\mathbf{b}} \cdot \nabla \times (\nabla \cdot \bar{\mathbf{R}}), \quad (42)$$

which contains the $E \times B$ drift only, although there are similar terms involving the diamagnetic drift and parallel velocity as well. The diamagnetic drift term could play a significant role, in particular for finite Larmor radius effects and poloidal flow generation, however, a full investigation which includes this term has been left for future studies. The parallel velocity term has a different nature, and it can be considered in the problem of toroidal flow generation which is not considered here, thus we ignore it in the present investigation. The $E \times B$ term, which we do investigate, is expected to provide a source for the generation of poloidal flows, as well, since the mean flow in our model, found by taking the time average of the continuity equation (33), is

$$-\frac{\partial \langle \Omega \rangle}{\partial t} + \langle (\mathbf{v}_E + \mathbf{v}_{pi} + v_{||} \hat{\mathbf{b}}) \cdot \nabla (\bar{n}_i - \Omega) \rangle = 0, \quad (43)$$

as the linear terms do not contribute to the mean flux, and the perturbed density acting on the divergence of the velocities is small.

It is worth noting that there are both quadratic and cubic terms which arise in (42)

$$\begin{aligned} S &= \mathbf{v}_E \cdot \nabla \Omega \\ &= \tau_{IC} R \{ \tilde{\phi}, \tilde{\Omega} \} \\ &= \tau_{IC} R \{ \tilde{\phi}, \nabla \cdot (n_{i0} \nabla_{\perp} \tilde{\phi}) \} + \tau_{IC} R \{ \tilde{\phi}, \nabla \cdot (\tilde{n}_i \nabla_{\perp} \tilde{\phi}) \} \\ &= S^{(2)} + S^{(3)}, \end{aligned} \quad (44)$$

however, we neglect the cubic component in our measurements of S , although terms of this type will play a role in Sec. VII A. There are no linear terms in S since there is no equilibrium potential, and thus no equilibrium vorticity as well. We restrict our calculation of S to the $n = 0$ term, since the multiplication of $\tilde{\phi}_n$ by itself can only result in harmonics with toroidal mode number 0 or $2n$. Our investigations of this term focus specifically on single- n simulations, thus the harmonic with mode number $2n$ is not simulated. Although the $n = 0$ term is measured, and will be discussed in the upcoming analysis, it does not act during these simulations since coupling with the equilibrium is neglected, as mentioned at the end of Sec. III B. We also note that at this time a number of factors relating to the generation of zonal flows have been neglected, particularly the role of heat flux effects related to the ion Landau damping and nonadiabatic electrons.⁶⁵ All of these effects will be considered in future investigations.

Several mechanisms of Reynolds stress and flow generation exist. In general, the sources of flow (and any finite Reynolds stress) can be viewed as a result of some symmetry breaking, leading the flow to favor one direction over the other. In the simplest case, a modulational instability of drift wave turbulence results from the presence of a large scale seed mode, which breaks the symmetry and causes the generation of large scale shear flows.^{33,66} Consequently, the resulting Reynolds stress is proportional to the derivatives of the seed flow and the amplitude of the small scale turbulence intensity. This leads the modulational instability to have the character of a negative diffusion instability. In other mechanisms, the symmetry breaking may occur due to asymmetry of the eigenmode structure (i.e., ballooning angle),

e.g., due to the turbulence intensity gradient.⁶⁷ These mechanisms do not depend on the amplitude of the large scale flow (nor on its derivatives) and they are usually referred to as residual stresses (because they provide a source of momentum, even when the flow is zero). The symmetry of the eigenmode structure can also be broken by a number of geometrical effects such as up-down asymmetry of the divertor configurations^{68,69} or magnetic shear profile effects,⁷ as occurs here. In the coming analysis, we show that without any seed mode, and in a geometrically symmetric equilibrium, the developed Reynolds stress is found to possess not only the symmetric $m = 0$ term, but also asymmetric terms with finite m .

We begin with the consideration of Reynolds stress for a single localized mode, occurring in the low shear case. Figure 18(a) corresponds with the potential cross section shown in Fig. 5(a), and shows the development of finite Reynolds stress, due to the nonzero value of S . Although S grows in time, its structure is stationary throughout the linear growth phase. The overall structure is poloidally asymmetric with a local minima located on the poloidal midplane, which could be considered to align with the ballooning angle of $\theta_0 = 0$ (as is the case for the localized mode). This structure exhibits a middle region of one polarity, surrounded by regions of the opposite polarity which is indicative of this term being able to generate significant shear flows.

Considering the corresponding poloidal Fourier transform of S in Fig. 19(a), we find significant values of S for mode numbers $m \leq 3$. The significant amplitude of the poloidally symmetric, $m = 0$, component could lead to the generation of zonal flows, if coupling with the $n = 0$ harmonic was included. This observation demonstrates a novel effect of global tokamak geometry in the development of poloidal flows, however, one has to note that the actual value of rotation or flow would be affected by coupling and self-regulation due to the $n = 0$ mode which was not included in these simulations. We also see

the development of significant $m = 1$, and $m = 2$ components, the former of which could be implicated in GAMs, and in the development of the $m = 1$ flows seen recently in experiments.³⁴

For the ballooning mode structure, shown in Fig. 18(b) and corresponding with Fig. 5(b), there is a similar structure to what is shown in Fig. 18(a), however, this structure is obscured by a significant amount of short-radial-wavelength Reynolds stress, appearing dominantly on the HFS. This short-radial-wavelength Reynolds stress arises due to the fragmentation of the potential structure into a large number of small circular vortices, as we described for the low τ_{IC} case in Fig. 12(a). Indeed, the Reynolds stress corresponding to Fig. 12(b), shown in Fig. 20, appears without this short-radial-wavelength Reynolds stress, and clearly identifies a similar structure to that in Fig. 18(a), which will be identified as the banded structure. For the ballooning mode, the banded structure is significantly wider than for the localized mode, due to the larger radial extent of the ballooning mode, however, it still experiences a local minima which is aligned precisely with the ballooning angle. As the diamagnetic effects are increased, the banded structure loses its symmetry about the ballooning angle, and comes to possess only a single region of significant amplitude, as shown in Fig. 20. This suggests that the net shear flow would strongly favor a single poloidal direction.

Considering the poloidal Fourier transforms of S for the ballooning structure, Fig. 19(b) corresponding with Fig. 18(b), and Fig. 21 corresponding with Fig. 20, we see that the short-radial-wavelength Reynolds stress possesses a poloidal mode number of $m = 4$ and $m = 5$, as may be expected since its presence is dominant in the upper and lower HFS quadrants. The decomposition in Fig. 21 shares some similarities with Fig. 19(a), except that the $m = 0$ component experiences three peaks, rather than four, in the area above $\psi \approx 0.37$ overlapping with the other harmonics. As expected, considering the real and

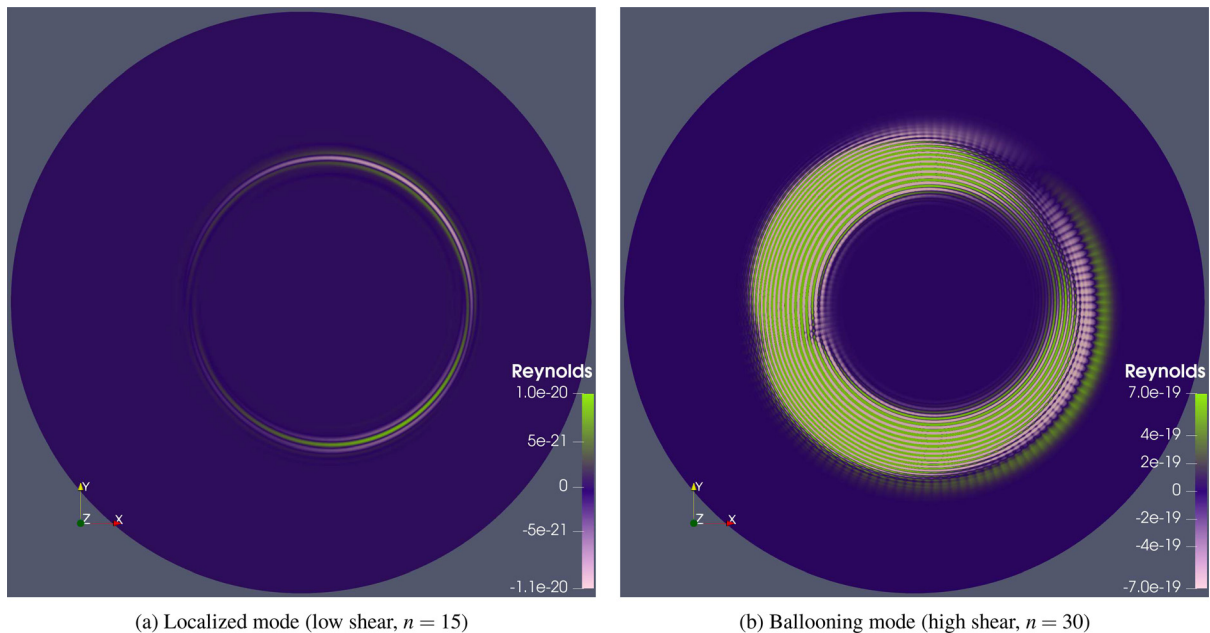


FIG. 18. Poloidal cross section of $S = \hat{\mathbf{b}} \cdot \nabla \times (\nabla \cdot \bar{\mathbf{R}})$ corresponding with the localized mode (a) and ballooning mode (b) in Fig. 5.

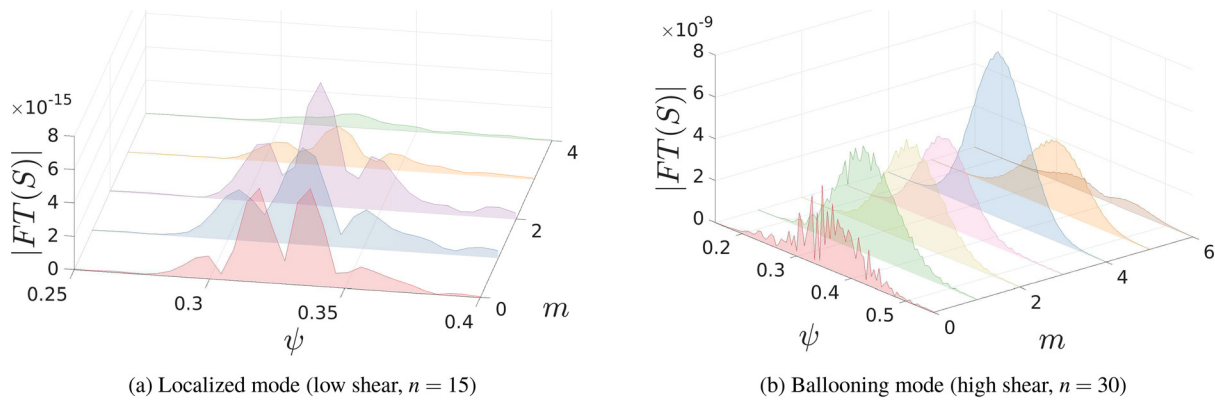


FIG. 19. Poloidal Fourier decomposition of $S = \hat{\mathbf{b}} \cdot \nabla \times (\nabla \cdot \bar{\mathbf{R}})$ corresponding with the localized mode (a) and ballooning mode (b) in Fig. 18.

imaginary components of this Fourier decomposition shows these three peaks to possess opposite polarity, and thus we can expect the development of significant flow shear in the regions between these peaks, when coupling to the $n=0$ mode is included. Figure 21 also shows the presence of two new peaks in harmonics $m=0$ and $m=1$ located at smaller radii. These portions are, of course, also relevant for zonal flows, GAMs, and the $m=1$ flows witnessed in Ref. 34.

VII. NONLINEAR SATURATION IN SINGLE- n AND MULTI- $n > 0$ SIMULATIONS

As we have mentioned, the simulations discussed in this paper do not include coupling of the ITG modes to the equilibrium ($n=0$)

state. Nevertheless, the interaction between finite- n ITG modes can still lead to nonlinear saturation via coupling to stable modes. Furthermore, it is of interest to observe the effects of global geometry and magnetic shear on the ITG modes themselves, before studying the much more complicated problem of how these modes interact-with and are affected-by an evolving equilibrium. Aside from saturation, the current investigations focus on the structure and the distribution of energy over the constituent toroidal harmonics, along with studying the nature of the turbulence generated. Simulations including coupling to $n=0$ will be completed in future investigations, which will search for the generation of $n=0$ zonal flows (which can be generated by our aforementioned Reynolds stress) and transport barrier formation. We also reserve more detailed nonlinear benchmarking with other codes such as BOUT++ for future investigations.

A. Single- n saturation due to non-Boussinesq Reynolds stress

Before we move on to results which include the interaction of multiple $n > 0$, it is interesting to note that saturation was actually obtained in the low magnetic shear cases using only a single toroidal

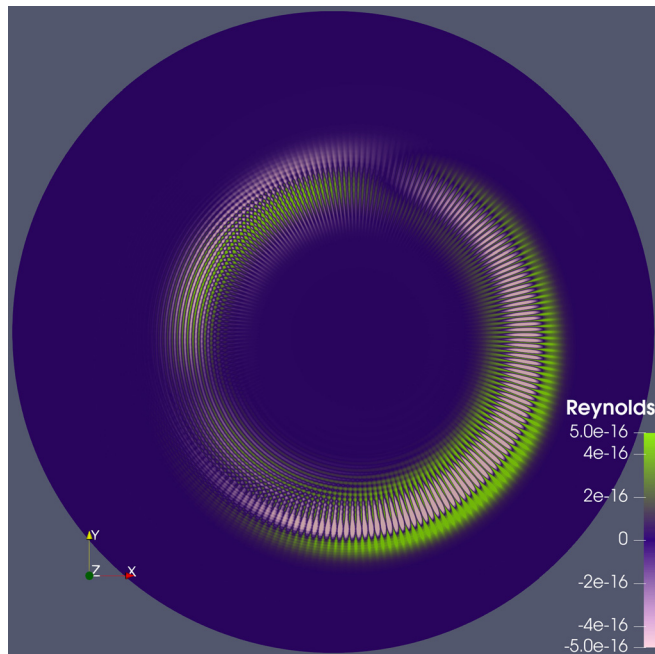


FIG. 20. Poloidal cross section of $S = \hat{\mathbf{b}} \cdot \nabla \times (\nabla \cdot \bar{\mathbf{R}})$ for $\tau_{IC} = 0.021$ showing the disappearance of the high radial wave vector S corresponding with the reduced mode fragmentation in Fig. 12(b).

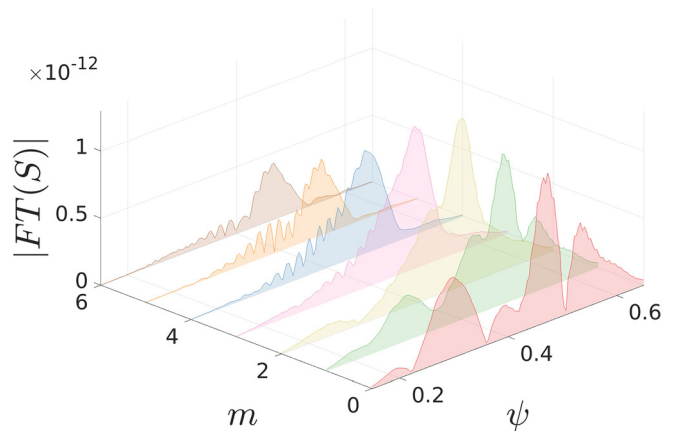
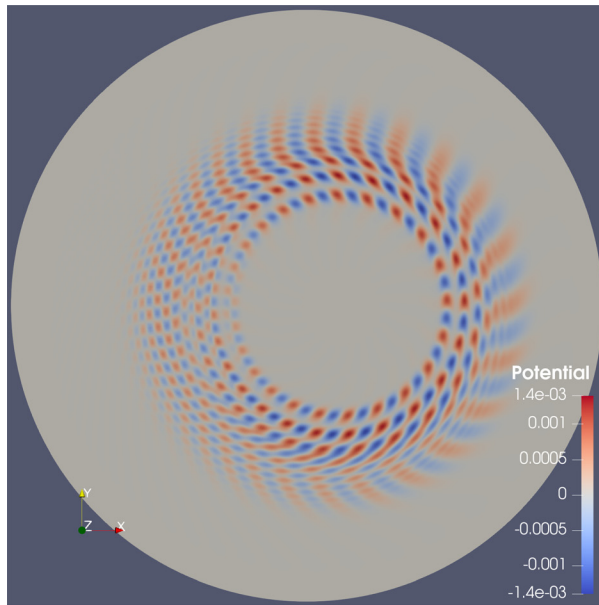
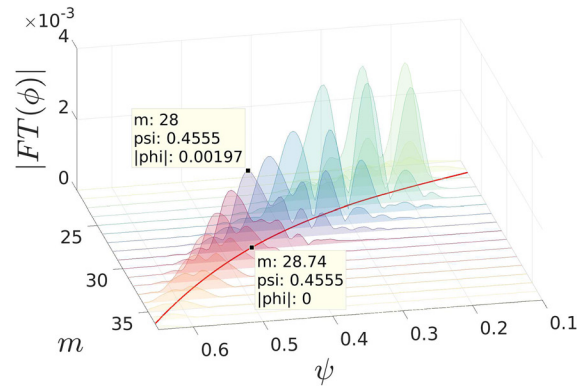


FIG. 21. Poloidal Fourier decomposition of $S = \hat{\mathbf{b}} \cdot \nabla \times (\nabla \cdot \bar{\mathbf{R}})$ for $\tau_{IC} = 0.021$.



(a) Poloidal cross section of ϕ



(b) Poloidal Fourier decomposition of ϕ

FIG. 22. Saturation of a single- n mode via coupling to stable m 's. These show the poloidal cross section (a) and poloidal Fourier decomposition (b) of ϕ , and are the late-time evolution of Figs. 7 and 14, respectively.

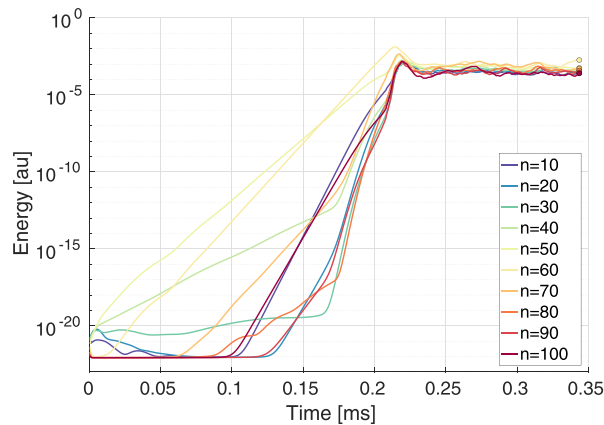
harmonic, n . This involves nonlinear coupling to stable poloidal, m , harmonics. The low-shear case is that which typically favors the localized mode, and although saturation was witnessed for all studied n 's, saturation occurs the easiest (i.e., with no reduction in the simulation time step) in low n simulations. Since nonlinear energy transfer with the $n=0$ mode has been precluded, this dissipation must occur through cubic coupling, which is only present in the density equation (33), and involves terms such as $S^{(3)}$ identified in (44). It must be highlighted that these terms exist specifically because we do not use the Boussinesq approximation when calculating the flux from the inertial drift. The coupling to stable m 's occurs through relations like $\partial \tilde{n}_{m-1}^n / \partial t \sim \tilde{\phi}_{m-1+1}^n \tilde{n}_{m-1}^{-n} \tilde{\phi}_{-m}^n$, where poloidal mode $m-1$ is the first stable mode below mode m . In this equation, the variable \tilde{n} is understood to represent \tilde{n}_i , and the subscript (superscript) designates the poloidal (toroidal) harmonic. As saturation is approached, we witness the development of localized modes at lower radii, and intensified ballooning modes at larger radii, as shown in Fig. 22(a), which is the late-time evolution of Fig. 7. This behavior can also be seen in Fig. 22(b), which can be compared to the pre-saturated state in Fig. 14, and shows the development of an additional localized mode along with a broader and more intense ballooning structure. These saturated states are not turbulent since every radial location favors a particular poloidal harmonic, based on the q -profile.

It is most likely that the stabilizing effect comes from the development of the localized modes at smaller radii, which can remain stable and absorb the energy of the neighboring modes.^{70,71} On the other hand, the increased radial extent of the ballooning portion merely absorbs additional harmonics into its structure, thereby destabilizing them through the constructive interference effect. For the higher shear cases, there is not enough room (between the neighboring rational

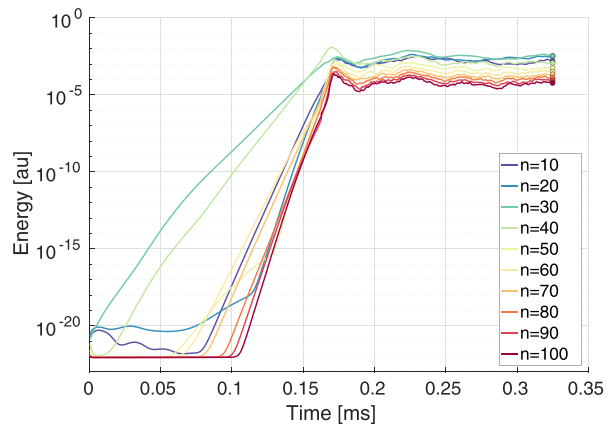
surfaces) to form the localized modes at smaller radii, and thus for the medium and high shear cases, we do not witness saturation in single n simulations.

B. Multiple $n > 0$ turbulent saturation

The low, medium, and high shear cases all attained saturation in nonlinear simulation of multiple n 's. A trace of the energy levels for each of the constituent toroidal harmonics for the low and high shear cases can be seen in Figs. 23(a) and 23(b), respectively. In these simulations, we included toroidal harmonics $n = 10, 20, 30, \dots, 100$. The energy levels of the saturated states are markedly different, with the high shear case retaining a strict hierarchy of energies for each n , whereas for the low shear case, the energies of individual n 's vary significantly, and frequently cross each other. It may be expected that this is a result of the increased q -profile for the high shear case, which has a value of approximately $q = 1.6$, at the center of the turbulence, in comparison to $q = 1.1$ for the low shear case. Thus, the change in m between each value of n varies more significantly (making it more difficult for m 's to couple), and the maximum m is larger for the high shear case (yielding more stable m 's above the stable ones). Nevertheless, if we change the simulated poloidal harmonics to $n = 7, 14, 21, \dots, 70$, thereby counteracting both of these effects, the energy levels of the high shear case still remain relatively distinct, although they are slightly pushed together. For both sets of simulated toroidal harmonics, the total energy of the high shear case is slightly larger than that of the low shear case. Finally, for comparison, the energy level for the single n saturation cases observed for low shear are slightly higher than the multiple n simulations, being centered around 1×10^{-3} , compared to around 5×10^{-4} , as shown in Fig.



(a) Low shear case, which typically favors localized/mixed modes.



(b) High shear case, which typically favors ballooning modes.

FIG. 23. Comparison of energy growth and saturation for low (a) and high (b) shear cases.

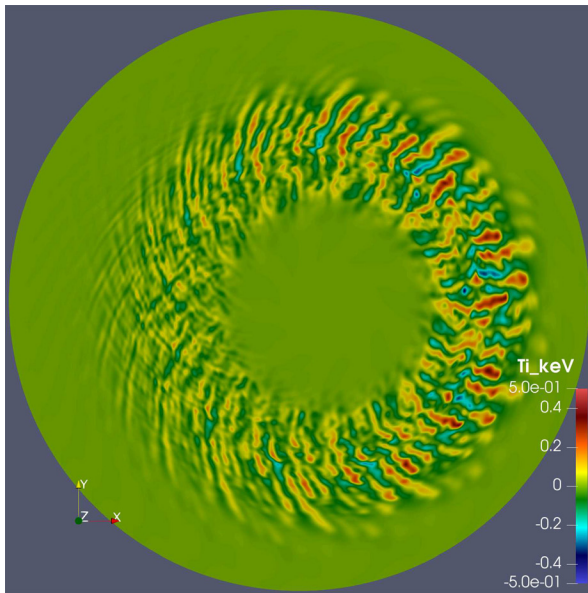
23(a). This identifies that energy coupling to stable modes occurs more easily for multiple n .

Poloidal cross sections of the temperature perturbations in the saturated state for the low and high shear cases are shown in Figs. 24(a) and 24(b). As the turbulent state is reached, the up-down asymmetry of the ballooning angle disappears, and the poloidal rotation ceases. For both cases of shear, the turbulence is much more active on the LFS, and exhibits a multi-stage burst behavior. High temperature vortices begin in an inner region, escape to a middle region (where they pause briefly to develop), then burst out to larger radii. The high shear case forms wider and more elongated structures, which tend to occur with a more consistent poloidal spacing. On the other hand,

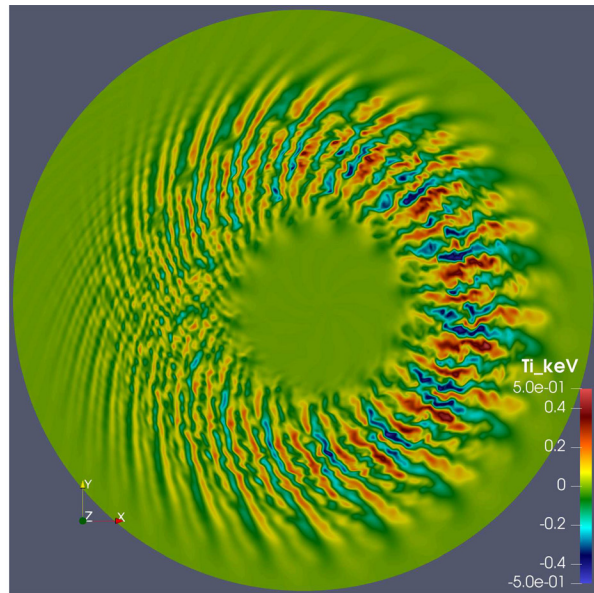
turbulence in the low shear case tends to be limited to a smaller radial extent, and form more circular vortices.

VIII. SUMMARY

This paper studies a fluid model of ion temperature gradient modes, and focuses on global simulations in realistic tokamak geometry. We have demonstrated the excitation of ITG modes in global geometry, with realistic equilibrium conditions, resulting in the formation of two characteristic mode structures arising from the differing density of rational surfaces. The localized mode structure is yet to be well documented, and the commonly considered ballooning mode structure was shown to exhibit nontrivial poloidal rotation due to



(a) Low shear case, which typically favors localized/mixed modes.



(b) High shear case, which typically favors ballooning modes.

FIG. 24. Poloidal cross section of perturbed temperature comparing the saturated states for low (a) and high (b) shear cases.

inhomogeneous plasma parameters in the gradient zone, along with an unexpected magnitude of radial shift from the rational surfaces. We have further shown the development of Reynolds stress structures which include multi-harmonic components, $n = 0, m = 0, 1, 2, \dots$ as a result of global parameter profiles and the global toroidal approach. Preliminary nonlinear results have shown characteristic differences in mode-energy depending on the magnetic shear.

Our model is composed of toroidal and slab components, and the analytic behavior of our local model was shown to exhibit some competition between the two components,⁴⁹ since the instability of the full model was lower than that of each component on its own (Fig. 2).

Following investigations of the local model, this model was then adapted into a global form for simulations using JOEKE. We began with successful benchmarking to the linear growth rate data in Refs. 31 and 32, and then showed the existence of two distinct eigenmode structures. The appearance of these structures depends on the spacing between rational surfaces, $\Delta = r/nq\hat{s}$, which can be varied through the magnetic shear, toroidal mode number, and q -profile.

Localized mode structures are formed directly between two adjacent rational surfaces, when the spacing between the surfaces is sparse (low shear, etc.). They are generated by the precise overlap of two poloidal Fourier harmonics, originating from the two neighboring rational surfaces. The Fourier amplitude of each poloidal harmonic goes to zero on the rational surfaces since the amplitude peaks on either side of the rational surface (arising when there are two adjacent localized modes) have opposite polarity. In the poloidal plane, the localized mode retains its symmetry about the midplane, and exhibits significant amplitude on the HFS identifying the importance of the sITG mechanism, which is still unstable on the HFS.

Ballooning mode structures are formed by strong coupling between many densely packed rational surfaces (high shear, etc.). Even though our equilibrium is poloidally symmetric, this mode develops an up-down asymmetry, enumerated by a finite ballooning angle, θ_0 , which causes the most radially symmetric vortex to be rotated to above the outboard midplane (opposite the direction of the diamagnetic drift). This asymmetry has been predicted within generalized 2D ballooning theory.^{1,3,7,8,20,21} The poloidal Fourier decomposition possesses a large number of overlapping peaks, forming the broad envelope characteristic of ballooning modes. Contrary to expectation, each peak in Fourier amplitude is formed at radii well above the corresponding rational surface. On average, each Fourier peak is shifted to larger radii by the distance of an entire rational surface. This shift has been discussed in terms of an imaginary component to the ballooning angle,^{7,61–63} however to our knowledge, such large values have never been considered.

For the ballooning structure, increasing the density of rational surfaces increases the prevalence of the tITG mechanism, as witnessed by the stabilization on the HFS. Along with increasing the diamagnetic effects, this provokes the involvement of more poloidal Fourier harmonics which experience more overlap and more shift. This leads to enhanced coupling, and a subsequently larger ballooning angle, and larger radial shift.

Contrary to the local model, increasing the magnetic shear was found to lead to larger growth rates. This is a global effect brought on by the constructive interference present in ballooning modes. For higher shear, there is more coupling between rational surfaces, and the modes are destabilized. Furthermore, since higher shear results from a stronger effect of plasma current in the equilibrium calculations, these

simulations also exhibited a decreased Shafranov shift. This allows the mode to spend more time in the unfavorable curvature region, thus further destabilizing the mode.

Although increasing the shear leads to an increased mode frequency in the local model, the resulting change in the global mode frequency was not as large. Furthermore, the frequency for the localized and ballooning modes was found to follow different trends. This shows that the frequency of the localized modes is more related to that of the local model, whereas the frequency of the ballooning modes is governed by the strong coupling between Fourier harmonics.

We found the generation of significant $n = 0$ Reynolds stress for all simulations. This stress possessed a substantial $m = 0$ component, which can be related to the generation of zonal flows, along with significant $m = 1$ and $2 \leq m \leq 5$ components, the former of which can be implicated in GAMs and the formation of poloidal convective cells, which were recently found in experiments.³⁴ For $m \leq 3$, the Reynolds stress possessed a radially banded structure with a middle region of one polarity, surrounded by regions of opposite polarity. This can lead to the development of significant shear flows when coupling to the equilibrium is included in future simulations.

Nonlinear saturation was found to occur due to several mechanisms. Interestingly, for simulations of a single toroidal harmonic, the low shear cases were all found to saturate via cubic coupling arising from a non-Boussinesq form of the vorticity, which coupled unstable m harmonics to stable ones. In simulations of multiple $n > 0$, all cases were found to reach turbulent saturation via more typical quadratic coupling of unstable n harmonics to stable ones. Under high shear, the energy levels of the constituent n harmonics all remained at distinct levels, whereas for low shear, the energy levels of each constituent n frequently crossed each other.

Overall, our results demonstrate the importance of global effects on micro-instabilities, in particular, on the mode saturation and Reynolds stress generation. Nonlinear simulations of ITGs within global codes such as JOEKE open up the pathway for studies of interactions of small scale turbulence with large scale MHD type phenomena such as self-generated and neoclassical shear flows, ELMs, the influence of Resonant Magnetic Perturbations (RMPs), and magnetic separatrix geometry on small scale instabilities.

ACKNOWLEDGMENTS

This work was supported by a Government of Canada NSERC Grant, Mitacs Globalink Research Award, and EUROFUSION Grant No. CfP-WP19-ENR-01/MPG-03. This work has also benefited from HPC resources from CINECA Marconi-Fusion, Project Nos. FUA32_JOEKE3D and FUA33_JOEKE3DE. The views and opinions expressed herein do not necessarily reflect those of the European Commission.

DATA AVAILABILITY

The data that support the findings of this study are available from the corresponding author upon reasonable request.

REFERENCES

1. T. Xie, H. Qin, Y. Z. Zhang, and S. M. Mahajan, "The unified ballooning theory with weak up-down asymmetric mode structure and the numerical studies," *Phys. Plasmas* **23**, 042514 (2016).

- ²P. Manz, A. Stegmeir, B. Schmid, T. T. Ribeiro, G. Birkenmeier, N. Fedorczak, S. Garland, K. Hallatschek, M. Ramisch, and B. D. Scott, "Magnetic configuration effects on the Reynolds stress in the plasma edge," *Phys. Plasmas* **25**, 072508 (2018).
- ³P. A. Abdoul, D. Dickinson, C. M. Roach, and H. R. Wilson, "Generalised ballooning theory of two-dimensional tokamak modes," *Plasma Phys. Controlled Fusion* **60**, 025011 (2018).
- ⁴P. Migliano, Y. Camenen, F. J. Casson, W. A. Hornsby, and A. G. Peeters, "Ion temperature gradient instability at sub-Larmor radius scales with non-zero ballooning angle," *Phys. Plasmas* **20**, 022101 (2013).
- ⁵R. Singh, S. Brunner, R. Ganesh, and F. Jenko, "Finite ballooning angle effects on ion temperature gradient driven mode in gyrokinetic flux tube simulations," *Phys. Plasmas* **21**, 032115 (2014).
- ⁶T. Xie, Y. Z. Zhang, S. M. Mahajan, and A. K. Wang, "Ballooning theory of the second kind-two dimensional tokamak modes," *Phys. Plasmas* **19**, 072105 (2012).
- ⁷X. Garbet, Y. Asahi, P. Donnel, C. Ehrlicher, G. Dif-Pradalier, P. Ghendrih, V. Grandgirard, and Y. Sarazin, "Impact of poloidal convective cells on momentum flux in tokamaks," *New J. Phys.* **19**, 015011 (2017).
- ⁸P. A. Abdoul, D. Dickinson, C. M. Roach, and H. R. Wilson, "Using a local gyrokinetic code to study global ion temperature gradient modes in tokamaks," *Plasma Phys. Controlled Fusion* **57**, 065004 (2015).
- ⁹J. Y. Kim, Y. Kishimoto, M. Wakatani, and T. Tajima, "Poloidal shear flow effect on toroidal ion temperature gradient mode: A theory and simulation," *Phys. Plasmas* **3**, 3689–3695 (1996).
- ¹⁰A. Bottino, A. G. Peeters, O. Sauter, J. Vaclavik, and L. Villard, "Simulations of global electrostatic microinstabilities in ASDEX upgrade discharges," *Phys. Plasmas* **11**, 198–206 (2004).
- ¹¹V. Grandgirard, Y. Sarazin, P. Angelino, A. Bottino, N. Crouseilles, G. Darmet, G. Dif-Pradalier, X. Garbet, P. Ghendrih, S. Jolliet, G. Latu, E. Sonnendrücker, and L. Villard, "Global full-f gyrokinetic simulations of plasma turbulence," *Plasma Phys. Controlled Fusion* **49**, B173–B182 (2007).
- ¹²V. Grandgirard, Y. Sarazin, X. Garbet, G. Dif-Pradalier, P. Ghendrih, N. Crouseilles, G. Latu, E. Sonnendrücker, N. Besse, and P. Bertrand, "GYSELA, a full-f global gyrokinetic semi-Lagrangian code for ITG turbulence simulations," *AIP Conf. Proc.* **871**, 100–111 (2006).
- ¹³G. Dif-Pradalier, V. Grandgirard, Y. Sarazin, X. Garbet, P. Ghendrih, and P. Angelino, "On the influence of initial state on gyrokinetic simulations," *Phys. Plasmas* **15**, 042315 (2008).
- ¹⁴B. F. McMillan, S. Jolliet, T. M. Tran, L. Villard, A. Bottino, and P. Angelino, "Avalanchelike bursts in global gyrokinetic simulations," *Phys. Plasmas* **16**, 022310 (2009).
- ¹⁵L. Villard, A. Bottino, O. Sauter, and J. Vaclavik, "Radial electric fields and global electrostatic microinstabilities in tokamaks and stellarators," *Phys. Plasmas* **9**, 2684–2691 (2002).
- ¹⁶B. Zhu, M. Francisquez, and B. N. Rogers, "GDB: A global 3D two-fluid model of plasma turbulence and transport in the tokamak edge," *Comput. Phys. Commun.* **232**, 46–58 (2018).
- ¹⁷P. Ricci and B. N. Rogers, "Plasma turbulence in the scrape-off layer of tokamak devices," *Phys. Plasmas* **20**, 010702 (2013).
- ¹⁸R. D. Sydora, V. K. Decyk, and J. M. Dawson, "Fluctuation-induced heat transport results from a large global 3D toroidal particle simulation model," *Plasma Phys. Controlled Fusion* **38**, A281–A294 (1996).
- ¹⁹X. Garbet, Y. Idomura, L. Villard, and T. Watanabe, "Gyrokinetic simulations of turbulent transport," *Nucl. Fusion* **50**, 043002 (2010).
- ²⁰T. Xie, Y. Z. Zhang, S. M. Mahajan, Z. Y. Liu, and H. He, "The Reynolds stress induced by weakly up-down asymmetric ion temperature gradient mode," *Phys. Plasmas* **23**, 102313 (2016).
- ²¹Y. Z. Zhang and S. M. Mahajan, "Reynolds stress of localized toroidal modes," *Phys. Plasmas* **2**, 4236–4245 (1995).
- ²²M. Becoulet, G. Huysmans, Y. Sarazin, X. Garbet, P. Ghendrih, F. Rimini, E. Joffrin, X. Litaudon, P. Monier-Garbet, J. M. Ane, P. Thomas, A. Grosman, V. Parail, H. Wilson, P. Lomas, P. DeVries, K. D. Zastrow, G. F. Matthews, J. Lonnroth, S. Gerasimov, S. Sharapov, M. Gryaznevich, G. Counsell, A. Kirk, M. Valovic, R. Buttery, A. Loarte, G. Saibene, R. Sartori, A. Leonard, P. Snyder, L. L. Lao, P. Ghil, T. E. Evans, R. A. Moyer, Y. Kamada, A. Chankin, N. Oyama, T. Hatae, N. Asakura, O. Tudisco, E. Giovannozzi, F. Crisanti, C. P. Perez, H. R. Koslowski, T. Eich, A. Sips, L. Horton, A. Hermann, P. Lang, J. Stober, W. Suttrop, P. Beyer, S. Saarelma, and J.-E. Workprogramme, "Edge localized mode physics and operational aspects in tokamaks," *Plasma Phys. Controlled Fusion* **45**, A93–A113 (2003).
- ²³M. Becoulet, F. Orain, P. Maget, N. Mellet, X. Garbet, E. Nardon, G. T. A. Huysmans, T. Casper, A. Loarte, P. Cahyna, A. Smolyakov, F. L. Waelbroeck, M. Schaffer, T. Evans, Y. Liang, O. Schmitz, M. Beurskens, V. Rozhansky, and E. Kaveeva, "Screening of resonant magnetic perturbations by flows in tokamaks," *Nucl. Fusion* **52**, 054003 (2012).
- ²⁴A. Monnier, G. Fuhr, P. Beyer, F. A. Marcus, S. Benkadda, and X. Garbet, "Penetration of resonant magnetic perturbations in turbulent edge plasmas," *Nucl. Fusion* **54**, 064018 (2014).
- ²⁵P. Beyer, S. Benkadda, G. Fuhr-Chaudier, X. Garbet, P. Ghendrih, and Y. Sarazin, "Turbulence simulations of transport barrier relaxations in tokamak edge plasmas," *Plasma Phys. Controlled Fusion* **49**, 507–523 (2007).
- ²⁶P. Beyer, F. de Solminihac, M. Leconte, X. Garbet, F. L. Waelbroeck, A. I. Smolyakov, and S. Benkadda, "Turbulence simulations of barrier relaxations and transport in the presence of magnetic islands at the tokamak edge," *Plasma Phys. Controlled Fusion* **53**, 054003 (2011).
- ²⁷L. Chôné, P. Beyer, Y. Sarazin, G. Fuhr, C. Bourdelle, and S. Benkadda, "L-H transition dynamics in fluid turbulence simulations with neoclassical force balance," *Phys. Plasmas* **21**, 070702 (2014).
- ²⁸L. Chôné, P. Beyer, Y. Sarazin, G. Fuhr, C. Bourdelle, and S. Benkadda, "Mechanisms and dynamics of the external transport barrier formation in non-linear plasma edge simulations," *Nucl. Fusion* **55**, 073010 (2015).
- ²⁹M. Han, Z.-X. Wang, J. Dong, and H. Du, "Multiple ion temperature gradient driven modes in transport barriers," *Nucl. Fusion* **57**, 046019 (2017).
- ³⁰W. Wang, W. Zhongxiong, L. Jiquan, Y. Kishimoto, J. Dong, and S. Zheng, "Magnetic-island-induced ion temperature gradient mode: Landau damping, equilibrium magnetic shear and pressure flattening effects," *Plasma Sci. Technol.* **20**, 075101 (2018).
- ³¹A. M. Dimits, G. Bateman, M. A. Beer, B. I. Cohen, W. Dorland, G. W. Hammett, C. Kim, J. E. Kinsey, M. Kotschenreuther, A. H. Kritiz, L. L. Lao, J. Mandrekas, W. M. Nevins, S. E. Parker, A. J. Redd, D. E. Shumaker, R. Sydora, and J. Weiland, "Comparisons and physics basis of tokamak transport models and turbulence simulations," *Phys. Plasmas* **7**, 969–983 (2000).
- ³²X. Lapillonne, S. Brunner, T. Dannert, S. Jolliet, A. Marinoni, L. Villard, T. Görler, F. Jenko, and F. Merz, "Clarifications to the limitations of the s - z equilibrium model for gyrokinetic computations of turbulence," *Phys. Plasmas* **16**, 032308 (2009).
- ³³P. H. Diamond, S.-I. Itoh, K. Itoh, and T. S. Hahm, "Zonal flows in plasma—A review," *Plasma Phys. Controlled Fusion* **47**, R35–R161 (2005).
- ³⁴L. Vermare, P. Hennequin, Ö. D. Gürçan, X. Garbet, C. Honoré, F. Clairet, J. C. Giacalone, P. Morel, A. Storelli, and T. S. Team, "Poloidal asymmetries of flows in the Tore Supra tokamak," *Phys. Plasmas* **25**, 020704 (2018).
- ³⁵T. Xie, Y. Z. Zhang, S. M. Mahajan, F. Wu, H. D. He, and Z. Y. Liu, "The two-dimensional kinetic ballooning theory for trapped electron mode in tokamak," *Phys. Plasmas* **26**, 022503 (2019).
- ³⁶A. Stegmeir, A. Ross, T. Body, M. Francisquez, W. Zholobenko, D. Coster, O. Maj, P. Manz, F. Jenko, B. N. Rogers, and K. S. Kang, "Global turbulence simulations of the tokamak edge region with GRILLIX," *Phys. Plasmas* **26**, 052517 (2019).
- ³⁷B. Coppi and F. Pegoraro, "Theory of the ubiquitous mode," *Nucl. Fusion* **17**, 969–993 (1977).
- ³⁸W. Horton, D. Choi, and W. M. Tang, "Toroidal drift modes driven by ion pressure gradients," *Phys. Fluids* **24**, 1077–1085 (1981).
- ³⁹H. Nordman, J. Weiland, and A. Jarmén, "Simulation of toroidal drift mode turbulence driven by temperature gradients and electron trapping," *Nucl. Fusion* **30**, 983 (1990).
- ⁴⁰S. Guo and J. Weiland, "Analysis of eta i mode by reactive and dissipative descriptions and the effects of magnetic q and negative shear on the transport," *Nucl. Fusion* **37**, 1095–1107 (1997).
- ⁴¹W. Horton and R. D. Estes, "Fluid simulation of ion pressure gradient driven drift modes," *Plasma Phys.* **22**, 663–678 (1980).
- ⁴²B. Coppi, M. N. Rosenbluth, and R. Z. Sagdeev, "Instabilities due to temperature gradients in complex magnetic field configurations," *Phys. Fluids* **10**, 582–587 (1967).

- ⁴³F. Romanelli, "Ion temperature-gradient-driven modes and anomalous ion transport in tokamaks," *Phys. Fluids B* **1**, 1018–1025 (1989).
- ⁴⁴S. C. Guo and F. Romanelli, "The linear threshold of the ion-temperature-gradient-driven mode," *Phys. Fluids B* **5**, 520–533 (1993).
- ⁴⁵G. W. Hammett and F. W. Perkins, "Fluid moment models for Landau damping with application to the ion-temperature-gradient instability," *Phys. Rev. Lett.* **64**, 3019–3022 (1990).
- ⁴⁶B. Scott, "Derivation via free energy conservation constraints of gyrofluid equations with finite-gyroradius electromagnetic nonlinearities," *Phys. Plasmas* **17**, 102306 (2010).
- ⁴⁷F. L. Hinton and C. W. Horton, "Amplitude limitation of a collisional drift wave instability," *Phys. Fluids* **14**, 116–123 (1971).
- ⁴⁸S. Braginskii, "Transport processes in a plasma," *Rev. Plasma Phys.* **1**, 205 (1965).
- ⁴⁹B. D. Scott, "Drift wave versus interchange turbulence in tokamak geometry: Linear versus nonlinear mode structure," *Phys. Plasmas* **12**, 062314 (2005).
- ⁵⁰G. Huysmans and O. Czarny, "MHD stability in x-point geometry: Simulation of ELMs," *Nucl. Fusion* **47**, 659–666 (2007).
- ⁵¹F. Orain, M. Bécoulet, G. Dif-Pradalier, G. Huijsmans, S. Pamela, E. Nardon, C. Passeron, G. Latu, V. Grandgirard, A. Fil, A. Ratnani, I. Chapman, A. Kirk, A. Thornton, M. Hoelzl, and P. Cahyna, "Non-linear magnetohydrodynamic modeling of plasma response to resonant magnetic perturbations," *Phys. Plasmas* **20**, 102510 (2013).
- ⁵²A. Fil, E. Nardon, M. Hoelzl, G. T. A. Huijsmans, F. Orain, M. Bécoulet, P. Beyer, G. Dif-Pradalier, R. Guirlet, H. R. Koslowski, M. Lehnen, J. Morales, S. Pamela, C. Passeron, C. Reux, and F. Saint-Laurent, "Three-dimensional non-linear magnetohydrodynamic modeling of massive gas injection triggered disruptions in JET," *Phys. Plasmas* **22**, 062509 (2015).
- ⁵³X. Garbet and R. E. Waltz, "Heat flux driven ion turbulence," *Phys. Plasmas* **5**, 2836–2845 (1998).
- ⁵⁴J. W. Connor, R. J. Hastie, and J. B. Taylor, "Shear, periodicity, and plasma ballooning modes," *Phys. Rev. Lett.* **40**, 396–399 (1978).
- ⁵⁵J. W. Connor and J. B. Taylor, "Ballooning modes or Fourier modes in a toroidal plasma?," *Phys. Fluids* **30**, 3180–3185 (1987).
- ⁵⁶J. Manickam, N. Pomphrey, and A. Todd, "Ideal MHD stability properties of pressure driven modes in low shear tokamaks," *Nucl. Fusion* **27**, 1461–1472 (1987).
- ⁵⁷L. A. Charlton, R. J. Hastie, and T. C. Hender, "Resistive 'infernal' modes," *Phys. Fluids B* **1**, 798–803 (1989).
- ⁵⁸H. Holties, G. Huysmans, J. Goedbloed, W. Kerner, V. Parail, and F. Soldner, "Stability of infernal and ballooning modes in advanced tokamak scenarios," *Nucl. Fusion* **36**, 973–986 (1996).
- ⁵⁹V. Dagnelie, "Dynamics of linear ITG modes with flow shear in ballooning space," Master's thesis (Utrecht University, 2017).
- ⁶⁰H. Wilson, P. Buxton, and J. Connor, "The effect of flow on ideal magnetohydrodynamic ballooning instabilities: A tutorial," in *Rotation and Momentum Transport in Magnetized Plasmas*, edited by P. Diamond, X. Garbet, P. Ghendrih, and Y. Sarazin (World Scientific, 2014), Vol. 2, Chap. 5, pp. 137–163.
- ⁶¹J. Kesner, "Effects of equilibrium on instabilities driven by ion temperature gradients in tokamaks," *Nucl. Fusion* **31**, 511 (1991).
- ⁶²Z. X. Lu, E. Fable, W. A. Hornsby, C. Angioni, A. Bottino, P. Lauber, and F. Zonca, "Symmetry breaking of ion temperature gradient mode structure: From local to global analysis," *Phys. Plasmas* **24**, 042502 (2017).
- ⁶³F. Zonca and L. Chen, "Theory of continuum damping of toroidal Alfvén eigenmodes in finite β tokamaks," *Phys. Fluids B* **5**, 3668–3690 (1993).
- ⁶⁴A. Smolyakov, X. Garbet, G. Falchetto, and M. Ottaviani, "Multiple polarization of geodesic curvature induced modes," *Phys. Lett. A* **372**, 6750–6756 (2008).
- ⁶⁵D. A. St-Onge, "On non-local energy transfer via zonal flow in the Dimits shift," *J. Plasma Phys.* **83**, 905830504 (2017).
- ⁶⁶A. I. Smolyakov, P. H. Diamond, and M. V. Medvedev, "Role of ion diamagnetic effects in the generation of large scale flows in toroidal ion temperature gradient mode turbulence," *Phys. Plasmas* **7**, 3987–3992 (2000).
- ⁶⁷Ö. D. Gürçan, P. H. Diamond, P. Hennequin, C. J. McDevitt, X. Garbet, and C. Bourdelle, "Residual parallel Reynolds stress due to turbulence intensity gradient in tokamak plasmas," *Phys. Plasmas* **17**, 112309 (2010).
- ⁶⁸N. Fedorczak, P. Diamond, G. Tynan, and P. Manz, "Shear-induced Reynolds stress at the edge of L-mode tokamak plasmas," *Nucl. Fusion* **52**, 103013 (2012).
- ⁶⁹N. Fedorczak, P. Ghendrih, P. Hennequin, G. R. Tynan, P. H. Diamond, and P. Manz, "Dynamics of tilted eddies in a transversal flow at the edge of tokamak plasmas and the consequences for L-H transition," *Plasma Phys. Controlled Fusion* **55**, 124024 (2013).
- ⁷⁰P. W. Terry, D. A. Baver, and S. Gupta, "Role of stable eigenmodes in saturated local plasma turbulence," *Phys. Plasmas* **13**, 022307 (2006).
- ⁷¹K. D. Makwana, P. W. Terry, J.-H. Kim, and D. R. Hatch, "Damped eigenmode saturation in plasma fluid turbulence," *Phys. Plasmas* **18**, 012302 (2011).